Study of Magnetite Nanoparticle Assemblies Using X-ray Resonance Magnetic Scattering (XRMS)

Dalton Griner

A senior thesis submitted to the faculty of
Brigham Young University
In partial fulfillment of the requirements for the degree of

Bachelor of Science

Dr. Karine Chesnel, Advisor

Department of Physics and Astronomy

Brigham Young University

August 2016

ABSTRACT

Study of Magnetite Nanoparticle Assemblies Using X-ray Resonance Magnetic Scattering (XRMS)

Dalton Griner
Department of Physics and Astronomy
Brigham Young University
Bachelor of Science

Magnetic nanoparticle technology is changing the world with important applications in healthcare such as more effective cancer treatments and drug delivery systems. To understand the magnetic behavior of Fe_3O_4 (known as magnetite) nanoparticles when forming assemblies, we have studied them with x-ray diffraction techniques. We used organic solution methods to create nanoparticles with different particle sizes ranging from 5 to 11 nm. Using X-ray Diffraction (XRD) and Transmission Electron Microscopy (TEM), we finely measured the average particle size and distribution. Using the synchrotron at the Stanford Synchrotron Radiation Lightsource (SSRL) at Stanford Linear Accelerator Center (SLAC), X-ray Circular Magnetic Dichroism (XMCD) and X-ray Resonance Magnetic Scattering (XRMS) experiments were conducted at different temperatures and magnetic fields on the freshly made samples. From this data, spin and orbital magnetic moments, as well as magnetic profiles, were extracted that provide information about the magnetic order in the nanoparticle assembly and its dependency on particle size, concentration, and temperature.

Keywords: Magnetite, Nanoparticles, Magnetic Scattering, Magnetic Order, Synchrotron

ACKNOWLEDGEMENTS

I would like to express my profound gratitude for my mentor Dr. Karine Chesnel. Her countless hours, patience, and expertise made this thesis possible. I count my undergraduate research as being the best, and most enjoyable, part of my experience at Brigham Young University, and was made possible by the phenomenal mentoring of Dr. Chesnel. She provided me opportunities most undergraduates would never dream of having and helped me through every step of the learning experience. She has gone above and beyond what is expected of an advisor and words can't really express my appreciation for everything she has done. I would also like to thank the Physics and Astronomy Department, as well as the Stanford Synchrotron Radiation Lightsource (SSRL) for their contributions to this thesis. I express gratitude to my parents for supporting me and encouraging me to pursue my interests. Without them I would not have been able to accomplish anything. Finally, I thank my wonderful wife Kayleigh, who is the inspiration behind everything I do.

Contents

Chapter 1

Introduction

1.1 Background

Nanotechnology involves the study of materials at a very small scale and has become a buzzword in science with promises of seemingly endless applications. Magnetic nanoparticles are even a prominent topic in healthcare and the life sciences. Particularly relevant and exciting applications to me, as I seek a PhD in medical physics, are in cancer diagnosis and treatment. Due to their controllable physical and chemical properties, nanoparticles have a variety of roles in these fields. For example, in combination with strong magnetic fields, nanoparticles can be functionalized and directed to targeted cells for therapeutic effects [1].

Iron oxide nanoparticles are being used in what has been cited as the ever-promising "fourth leg" of cancer treatment known as magnetic hyperthermia treatment [2]. This experimental technique uses magnetic nanoparticles to transform electromagnetic energy from powerful external magnets to intense heat, effectively killing and shrinking cancerous tumor tissue. Active research is being conducted to improve this treatment and expand it to other sectors such as bacterial infections, drug delivery, and even the polymer industry [3].

In order to fulfill the lofty goals set by doctors, scientists, and corporations, the behavior of these nanoparticles needs to be fully understood. While the bulk properties of most materials used in these applications are well understood, these properties are influenced dramatically as these materials reach the nano-scale and can vary for small size variations. Our research, in part presented in this thesis, seeks to understand the magnetic behavior of Fe_3O_4, commonly known as magnetite, nanoparticle assemblies. Magnetite is advantageous as it is non-toxic to humans, can be highly functionalized, and remains in the bloodstream for an extended period of time [4], making it a great material for the many applications explained above.

To study the magnetic behavior of magnetite nanoparticles, we fabricated our own samples, using organic methods, which we then deposited on Si_3O_4 membranes in order to perform our experiments. Using TEM imaging we determined the average particle size of our samples. To gain understanding of the magnetic properties of our samples we used X-ray scattering techniques, specifically X-ray Magnetic Circular Dichroism (XMCD) and X-ray Resonance Magnetic Scattering (XRMS). To perform such sensitive measurements, we needed synchrotron x-ray radiation and we traveled to the Stanford Synchrotron Radiation Lightsource (SSRL). The synchrotron is an essential part of our experiment because it provides coherent,

polarized x-rays that can be tuned to specific energies. We varied the temperature and the external magnetic field to see their effects on our magnetic nanoparticle assemblies. The results we obtained provide interesting insights into the magnetic behavior of these nanoparticles that can eventually lead to better cancer therapies, among many other exciting applications.

1.2 Magnetic Properties of Fe_3O_4 Nanoparticles

Fe_3O_4 is comprised of two different iron ions, Fe^{3+} and Fe^{2+}. These two ions carry different magnetic moments. In Fe_3O_4, the moments carried by the Fe^{3+} and Fe^{2+} ions align in an antiparallel ordering and the opposing moments are unequal and a net magnetization remains [5]. This type of ordering is called ferrimagnetism. Magnetite is one of the oldest and most studied materials to exhibit ferrimagnetism. Magnetite nanoparticles are comprised of thousands of individual Fe_3O_4 molecules. Each of these molecules carries a net magnetic moment due to the ferrimagnetic behavior of the iron ions. The residual magnetic moments of the individual molecules tend to align so that the nanoparticle itself carries a combined magnetic moment, known as a macrospin. In a so-known superparamagnetic nanoparticle assembly, the macrospins of the individual particles are in a random order and in the absence of a magnetic field, the net magnetization is close to zero. However, in the presence of an external magnetic field, the macrospins of the nanoparticles tend to align with the external field. This effect is known as superparamagnetism. An illustration is given in Figure 1.1. When all of the macrospins align in an external field, the net magnetization is at a maximum. This point is called saturation.

The magnetic behavior of the nanoparticles can also be affected by temperature. At high temperatures the macrospins align randomly in a paramagnetic-like behavior. At lower

temperatures, below a so-called blocking temperature, the nanoparticles become magnetically blocked, or frozen. At this frozen state, the magnetic coupling between the particles is stronger and the particle spins tend to align even in the absence of a field [6]. The value of the blocking temperature strongly depends on the particle size, ranging from 30 K for the 5 nm particles, up to 170K for the 11 nm particles.

We conducted our experiments at various temperatures and magnetic fields to study these effects in more detail. The results are presented in later chapters of this thesis.

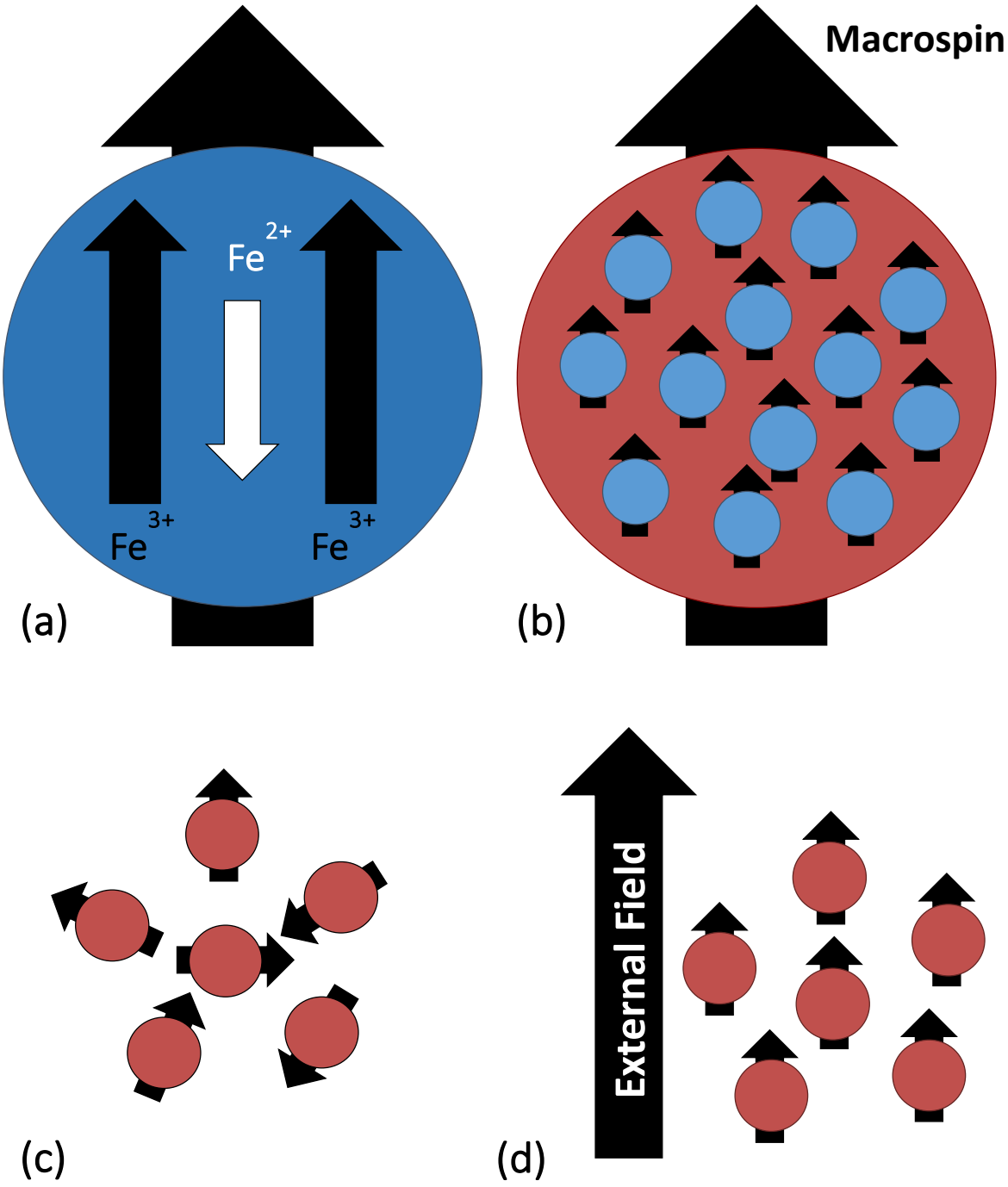

Figure 1.1 (a) Illustration of ferrimagnetism in a Fe_3O_4 unit. The opposing magnetic moments are unequal creating a net magnetic moment in the molecule. **(b)** Illustration of a macrospin present in a magnetite nanoparticle. The residual magnetic moments due to the ferromagnetic behavior of the Fe_3O_4 molecules align creating a net moment in the nanoparticle, creating a macrospin. **(c)** At high temperatures the macrospins of the nanoparticles are randomly oriented. **(d)** In the presence of an external magnetic field the individual macrospins align in an effect known as superparamagnetism.

Chapter 2

Magnetite Nanoparticle Synthesis

2.1 Creating Magnetite Nanoparticles

To understand the magnetic behavior of magnetite nanoparticle assemblies, we, in collaboration with Dr. Harrison of the Chemistry department of BYU, used organic methods to synthesize fresh Fe_3O_4 nanoparticles of various sizes. This method involves the thermal decomposition of an iron compound [7]. Wanting to study the effect of particle size we controlled certain parameters in the synthesis process to create samples of varying particle size. It has been observed that reaction temperature and reaction solutions can affect particle size [8]. We experimented varying these parameters and created three different sized nanoparticle sets that we will focus on in this thesis: NP16, NP17, and NP18. Samples sizes were determined with X-ray Diffraction (XRD) measurements and confirmed using Transmission Electron Microscopy (TEM).

The nanoparticles for set NP16 were created from a precursor, iron (III) oleate. This compound was created by slowly adding a methanol (CH_3OH) solution of sodium hydroxide (NaOH) to a methanol solution of $FeCl_3 \bullet 6H_20$ and oleic acid ($C_{18}H_{34}O_2$). This solution was filtered and dried under vacuum [9]. The nanoparticles were formed by mixing the iron (III) oleate in an oleic acid and octadecene ($C_{18}H_{36}$) solution that was then heated to 320 °C. The solution remained at this temperature for 30 min and cooled slowly to room temperature. The nanoparticles were precipitated with ethanol (C_2H_5OH) and isolated by centrifugation. The remaining solution was decanted and the magnetite nanoparticle precipitate was collected.

NP17 was created using another method beginning from an iron (III) acetylacetonate ($Fe(C_5H_7O_2)_3$) precursor [10]. This compound was mixed with hexadecane ($C_{16}H_{34}$), octadecene ($C_{18}H_{36}$), oleic acid ($C_{18}H_{34}O_2$), and oleylamine ($C_{18}H_{35}NH_2$). This solution was heated to 200 °C for 30 minutes and cooled slowly to room temperature. The nanoparticles were precipitated with ethanol and collected by centrifugation.

NP18 was prepared in the same manner as NP17 using diphenyl ether ($O(C_6H_5)_2$) in place of octadecene. Figure 2.1 shows the nanoparticle solution of NP18 heating inside of a fume hood.

After the nanoparticles were precipitated and collected they were deposited onto a Si_3N_4 membrane. The nanoparticles self-assembled and formed into roughly hexagonal lattices. By varying the concentration of the nanoparticle solutions deposited on the membranes we created a set of nine samples (see Table 2.1). The concentrations were varied in an attempt to achieve a monolayer deposition of the nanoparticles on the membrane. Different concentrations produced samples of varying interparticle distance, which will be discussed in subsequent chapters.

Figure 2.1 Image of our nanoparticle preparation. In this image the solution is being heated. Careful attention was given to temperature as this parameter controlled nanoparticle size.

2.2 Determining Particle Size

The size of the individual nanoparticles in our sets was measured using X-ray Diffraction (XRD) and Transmission Electron Microscopy (TEM). The measurements agreed between the different methods providing confidence in our size evaluation (see Table 2.1).

TEM is a technique in which a beam of electrons passes through a thin sample and is collected downstream after being scattered by the sample. It allows for higher resolution compared to optical telescopes and can image in the nanometer scale. Using a TEM microscope we imaged our samples (see Figure 2.2). Using the software package ImageJ, which determines the average diameter of an area selected, we circled every nanoparticle visible in the image of

our different samples to calculate an average particle diameter. We found NP16 to have a size distribution of 11.3 ± 2.5 nm, NP17 with a size distribution of 8.1 ± 1.7 nm, and NP18 with a size distribution of 5.6 ± 1.0 nm. XRD measurements were performed by Yanping Cai [11], and closely match the measurements taken with the TEM (see Table 2.1). Average particle size summary for our samples in found in Table 2.1.

	TEM (nm)	XRD (nm)	Samples
NP16	11.3 ± 2.5	11.0 ± 4.6	1, 2, 3
NP17	8.1 ± 1.7	8.5 ± 2.9	4, 5, 6
NP18	5.6 ± 1.0	5.8 ± 1.7	7, 8, 9

Table 2.1 Summary of nanoparticle statistical size and samples. Individual particle sizes were determined using two methods, XRD and TEM. The measurements agree between the two methods providing confidence in our size evaluation. A total of nine samples were created from the nanoparticles using different concentrations of our nanoparticle sets.

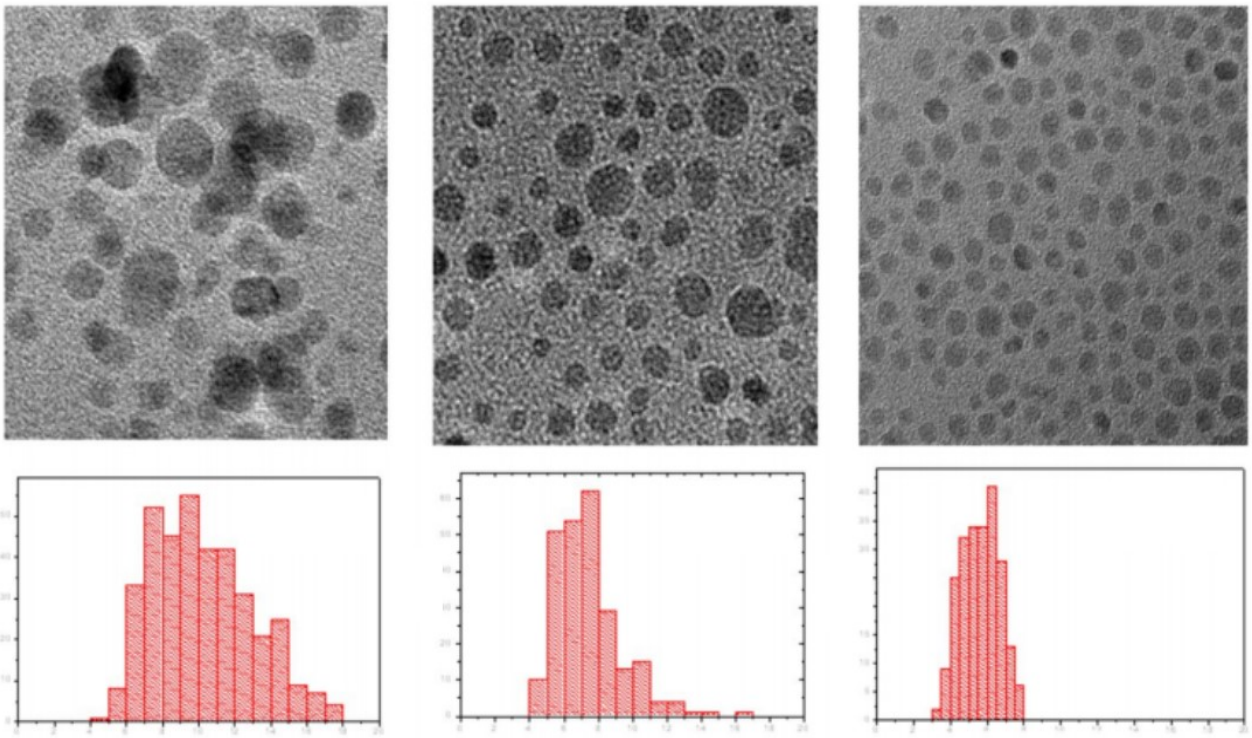

Figure 2.2 TEM images and size distributions for our nanoparticle samples. From left to right, NP16 with a size distribution of 11.3 ± 2.5 nm, NP17 with a size distribution of 8.1 ± 1.7 nm, and NP18 with a size distribution of 5.6 ± 1.0 nm. Figure taken from a publication by our group on nanoparticle synthesis [11].

Chapter 3

X-ray Magnetic Circular Dichroism (XMCD)

3.1 XMCD Overview

X-ray Absorption Spectroscopy (XAS) is a technique used to study the electronic composition and structure of a material. In an XAS experiment, x-rays pass through a material and the transmitted radiation is recorded using a photodiode. By comparing the initial intensity with the transmitted intensity as a function of the energy of the x-rays, structural information can be extracted.

An extension of XAS, the X-ray Magnetic Circular Dichroism (XMCD) technique measures the difference in absorption of a magnetic material caused by the switching of the polarization of the incident radiation. For transition metals the absorption can be measured at the L-edge. At that specific transition energy, the 2p electron is excited to the 3d state. As magnetic properties originate from the electronic spin configuration in the 3d state, this provides

information on the valence shell configuration of an atom and relates to the magnetic composition of the material.

In our experiment we seek to understand the magnetic properties of iron in its two ion forms, Fe^{2+} and Fe^{3+}. We measured our nanoparticle samples at the $L_{2,3}$ resonant edge energies, which originates from the 2p band splitting, $2p_{3/2}(l+s)$ and $2p_{1/2}(l-s)$, as a result of spin-orbit coupling. This leads to the L_2 and L_3 edges at approximately 707 eV and 720 eV respectively. The incident x-rays excite the electrons from the 2p band to the 3d band while conserving their initial spin. Due to the different spin orientations, absorption of the right and left polarized light will be different. This difference is what we study to better understand the magnetic properties of our samples.

3.2 Experimental Setup

The experimental setup we used to study our fabricated nanoparticles is outlined in Figure 3.1. A photo of the actual chamber with labeled parts is given in Figure 3.2. To perform the XAS and XMCD experiments we needed coherent, polarized x-rays we could tune at defined energies, specifically the energies of the L_2 and L_3 edges. To accomplish this, we traveled to the Stanford Synchrotron Radiation Lightsource (SSRL) located at the Stanford Linear Accelerator Center (SLAC). The synchrotron generates coherent x-rays that are polarized using an elliptical polarization undulator (EPU) into right and left circularly polarized soft x-rays. We recorded XAS spectra of our samples using a photodiode by scanning through the $L_{3,2}$ edges, from 690 eV to 735 eV. From these measurements we can extract meaningful magnetic data from our samples.

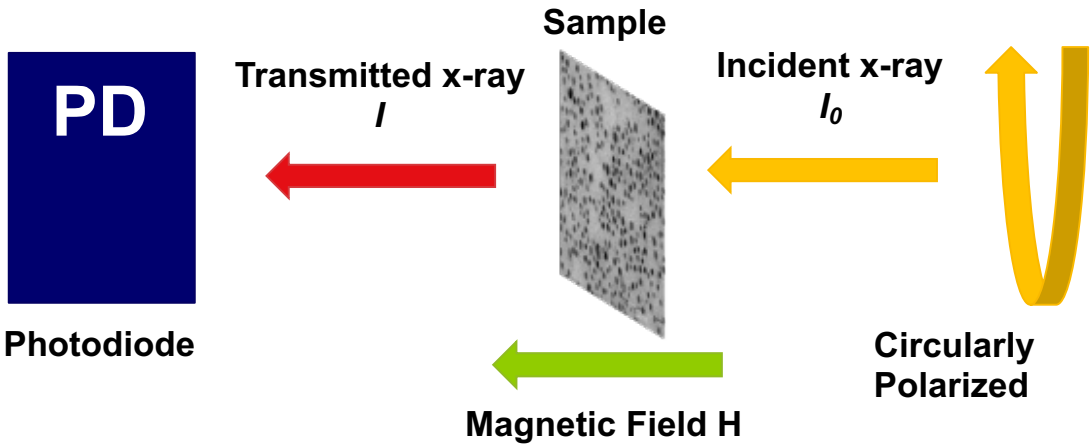

Figure 3.1 Outline of our XMCD experiment. Synchrotron radiation is elliptically polarized and passed through a sample in a magnetic field. The transmitted radiation is collected using a photodiode.

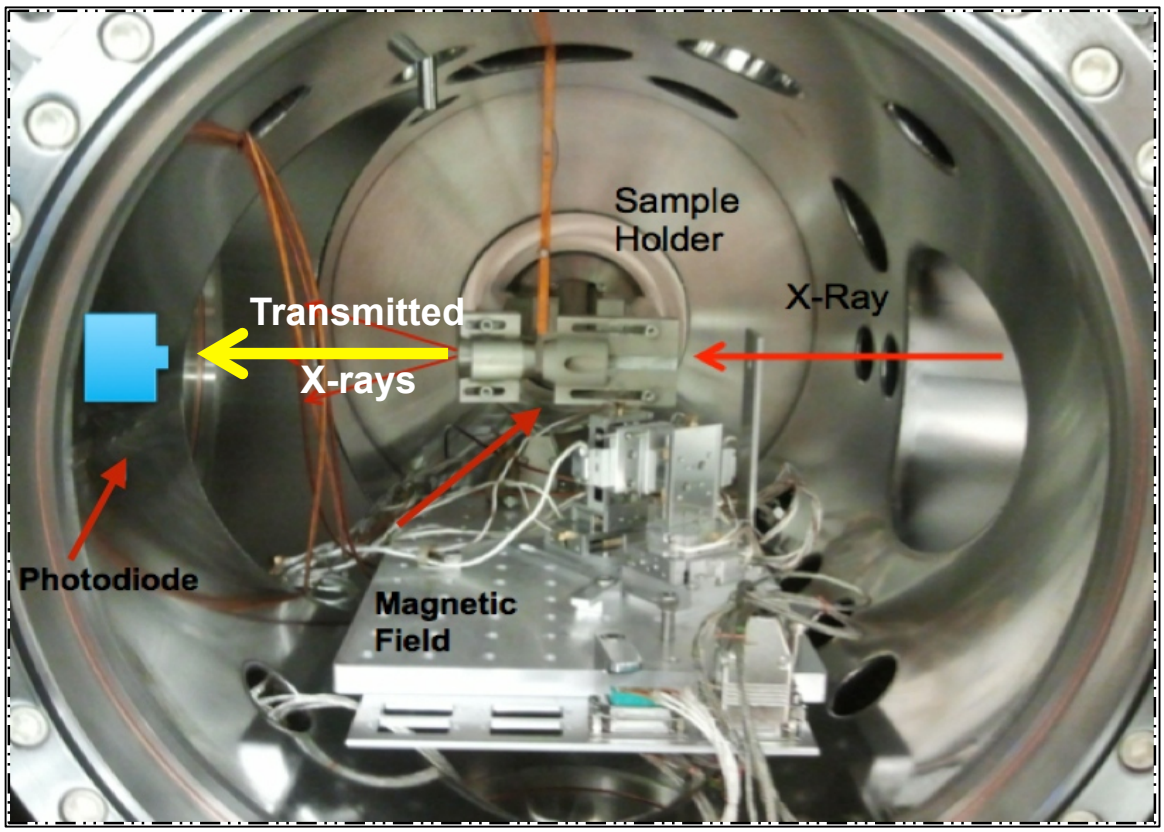

Figure 3.2 Photo of the vacuum chamber used for our XAS and XMCD measurements. Polarized x-rays enter from the right and pass through the sample. The sample is inserted in a magnetic field created by an electromagnet. The photodiode records the transmitted radiation.

3.3 XAS and XMCD Data

Using the synchrotron, we gathered XAS transmission spectra of our samples. The amount of transmitted light can be expressed into an amount of absorption *A* by using the incident intensity I_0 and transmitted intensity *I* in the following relation:

$$A = -\ln(T) \tag{3.1}$$

$$\text{where } T = \frac{I}{I_0}. \tag{3.2}$$

Peaks in a spectrum *A(E)* (absorption as a function of energy) indicate absorption edges. For our magnetite nanoparticles we measured at the L edge of iron, at around 707 eV (see Figure 3.3).

In a careful normalization process [6], the background slopes caused by charge absorption are subtracted to flatten the pre-edge and post-edge. In order to complete this, linear fits are applied. This ensures only the absorption peaks remain over a flat background. To generate an XMCD signal, the difference between the right and left absorption signals is taken. An example of a normalized absorption and XMCD curves for sample 3 are given in Figure 3.3.

Evident in the XMCD curve is the characteristic "W" shape with three distinct peaks (see Figure 3.4). This is a signature of magnetite (Fe_3O_4) as the peaks correspond to the antiparallel spins of the Fe^{2+} and Fe^{3+} ions. These peaks are referred to in this thesis as E_1 = 706 eV, E_2 = 707 eV, and E_3 = 708 eV. The determination of these energy values is useful for our later X-ray Resonant Magnetic Scattering (XRMS) experiments discussed in Chapter 4. The flip in sign passing from E_1 to E_2 and then on to E_3 is notable and a result we will be using later in our XRMS experimental analysis. Using the sum rules [6], the spin and orbital moments can be extracted which describe the magnetic properties of the material.

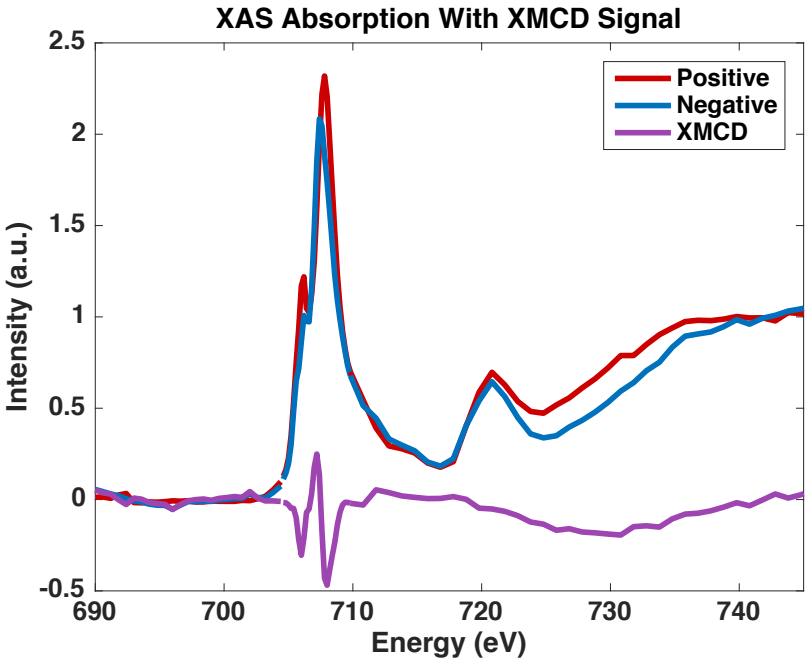

Figure 3.3 XAS absorption and XMCD curves for NP17 at 300 K. The red and blue curves correspond to right and left elliptically polarized x-rays scanned through the $L_{2,3}$ edges of iron. The purple XMCD curve is the difference of the absorption signals.

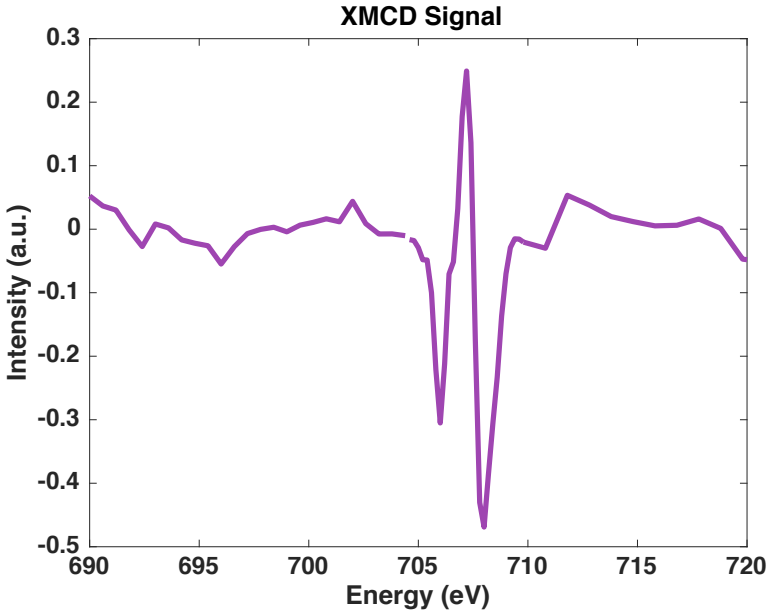

Figure 3.4 Zoomed in view of the characteristic "W" XMCD signature of iron. The "W" is created by the three magnetic moments contained in magnetite and the peaks correspond to the resonant energies of iron (706 eV, 707 eV, and 708 eV).

3.4 Conclusion

Using the XAS technique, structural information of a material can be studied. By using the difference in absorption of polarized x-rays, the XMCD provides information about the magnetic properties of a material. We conducted XAS and XMCD experiments on our magnetite nanoparticle assemblies and confirmed the presence of Fe^{2+} and Fe^{3+} ions present in a ferrimagnetic order. The characteristic "W" shape indicates the resonant energies at which our XRMS experiments need to later be conducted.

As the XMCD results are not the focus of this thesis, a brief overview was provided here for understanding and application to the XRMS experiments and results in subsequent chapters. For a more thorough explanation of the subject see published results by our group in [6].

Chapter 4

X-ray Resonance Magnetic Scattering (XRMS)

4.1 XRMS Technique Overview

X-ray Diffraction (XRD) is a technique used to study the atomic and molecular structure of an organized material. In this technique, the atoms (or molecules) scatter incident x-rays that are then captured using a CCD, film, or another similar device. By measuring the scattering angles and intensities, it is possible to create a three-dimensional picture of the electron density of the material being measured. From this electron density model, many properties can be studied and determined, most importantly, the structure of the material. XRD is correlated to charge scattering and was developed in the early 1900's.

Related to XRD is the more recent X-ray Resonance Magnetic Scattering (XRMS) technique. XRMS is used to study the magnetic order of materials, and was first theoretically developed by Platzman and Tzoar [12] and experimentally validated by Bergevin and Brunel in the 1970's [13]. Compared to charge scattering, non-resonant magnetic scattering signal is much

weaker and usually swallowed in the charge signal, making it more difficult to analyze. The XRMS technique exploits the enhancement of the magneto-optical contrast at the x-ray absorption edges, which allows for the weaker magnetic signal amplitude to be drastically increased.

Magnetic scattering is a result of the coupling between the photon spins and electron spins in a material and the resonant behavior is produced from an electric multi-pole transition. It has been experimentally observed that for transition metals resonance occurs the at $L_{2,3}$ edges [14].

4.2 Experimental Setup

The experimental setup which we used to study our fabricated nanoparticles is outlined in Figure 4.1. In June of 2013, June 2014, and February of 2015, we traveled to the Stanford Synchrotron Radiation Lightsource (SSRL) to conduct our experiments. The synchrotron was crucial to our experiment as it produces coherent x-rays whose energies and polarizations can be finely tuned. In order to study the magnetic effects of our samples we tuned the energy of the soft x-rays to the L_2 (approximately 721 eV) and L_3 (approximately 707 eV) edges of iron. A 2048 × 2048 pixel CCD camera was mounted on a three dimensional translational stage that allowed us to adjust the X, Y, and Z directions to best capture our scattering images.

In our study we seek to understand the effects of temperature and magnetic field on the magnetic ordering in the nanoparticle assemblies. To achieve this in our experiment, we used liquid helium and a cryostat to control temperatures, as well as a permanent magnet coupled with an electromagnet to produce varying magnetic fields. In our experiments we took images at temperatures ranging from approximately 10 K to 300 K. At a given temperature a sample was

imaged at various field values from -3000 G to 3000 G. Note that 3000 G is near the saturation field of sample 3.

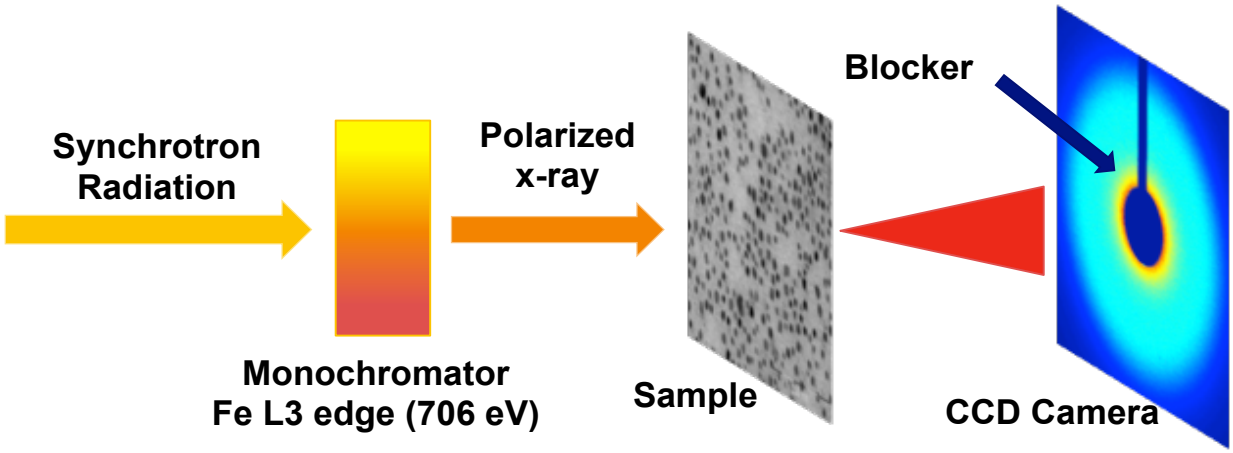

Figure 4.1 Outline of our XRMS experimental setup. Synchrotron radiation is tuned at required energy, polarized, and passed through nanoparticle sample. A CCD camera collects the resulting scattering image while a blocker absorbs the direct beam.

4.3 Generating Scattering Intensity Profiles

For this chapter the process of generating a magnetic profile and subsequent analysis will be outlined using data from sample 3 (NP16). The remainder of the results can be found in Chapter 5 of this thesis.

Figure 4.2 (a) is an experimentally obtained scattering image, the colors indicating photon counts, or radiation intensity. To extract information from the scattering image the two-dimensional image is converted into a one-dimensional intensity profile. This is accomplished by angularly integrating intensity, or photon counts, to create a radial profile.

The first step in creating a profile is to remove the shadow of the blocker put in place to protect the CCD camera from the direct beam. The average intensity is much lower in the shadow

and there is no meaningful information that can be gathered from this region, so it is "subtracted" it out of the image. This is accomplished by creating a mask, which replaces any shadowed region by zero. We created a program that generates a blocker by exploiting the difference in intensities of the shadow and remaining scattering image. The program is given a specific intensity cutoff, above which intensities are unchanged and below which intensities are zeroed. The shadowed pixels generally have intensities two to three orders of magnitude less than the remaining pixels so the cutoff is assigned a value near to, but above, the average of the shadowed pixels' average intensity. When the image and blocker are multiplied, the shadow intensities are zeroed and the remaining pixels are unchanged. Figure 4.2 (b) shows the corresponding mask generated for sample 3 in figure 4.2(a).

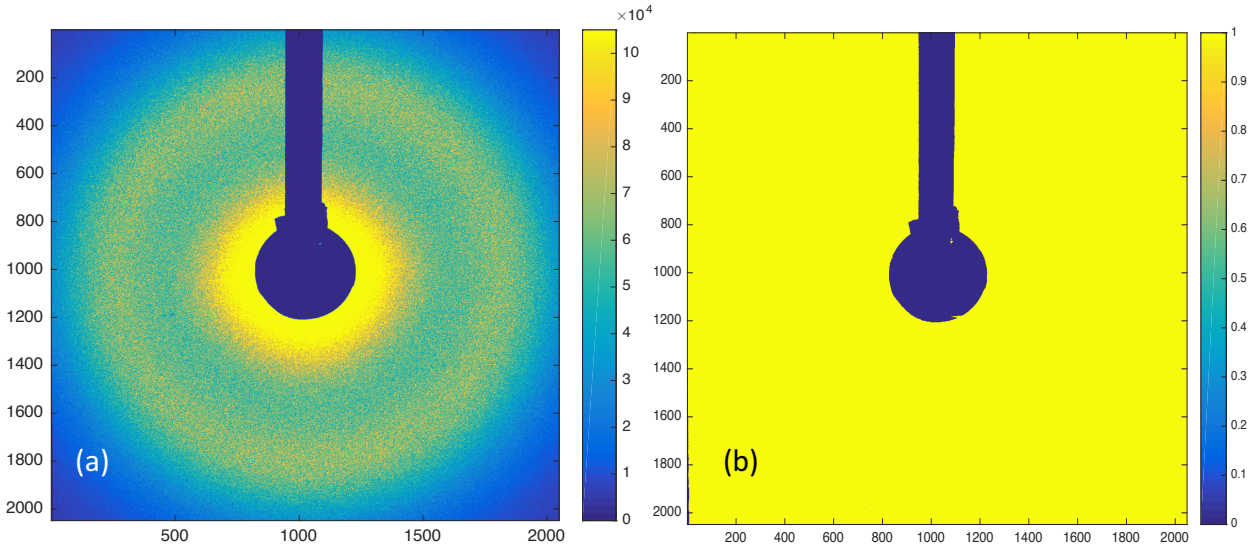

Figure 4.2 (a) Scattering image of sample 3 taken with a CCD camera at SSRL. The dark blue region in the center extending upwards is the shadow of the blocker. **(b)** Corresponding mask generated for scattering image in **(a)**. Dark blue pixels have a value of 0 while the yellow have a value of 1.

With the blocker effects eliminated is it possible to integrate intensity as a function of distance from the beam center. This is performed by creating concentric rings centered at the same position as the scattering image, with the width of each ring being set, here to eight pixels, as shown in Figure 4.3 and 4.4 (a). By selecting a ring at a specific radius and multiplying by the scattering image a specific area can be selected to integrate. The intensity is then integrated within this selected ring of the image.

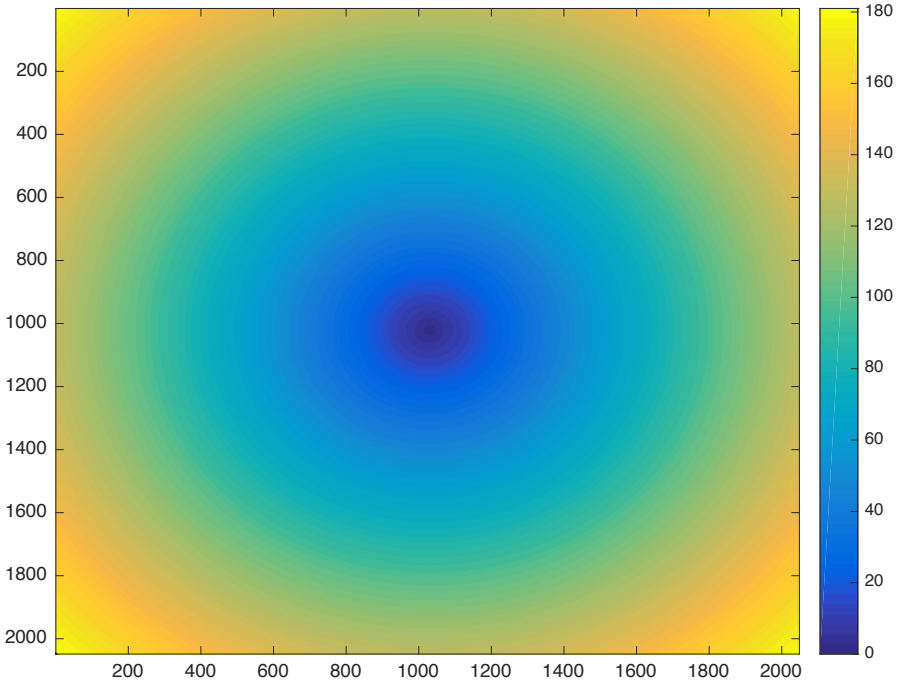

Figure 4.3 Concentric rings centered at the beam center with each ring having a width of eight pixels.

Next, two normalization steps are applied: a spatial normalization and a time normalization. The spatial normalization allows the profile to be produced in terms of the scattering vector q, which is essentially the distance from the center in the scattering pattern.

Time normalization consists in dividing the scattering signal by the intensity collected simultaneously on a gold mesh upstream of the sample.

Our scattering images are analyzed by producing a profile as a function of q. The scattering vector q is defined as: q = k' – k, or the resultant vector of the scattered and incident vector. The spatial normalization is applied by dividing the integrated pixel intensity by the angle α (see Figure 4.4 (a)), to prevent truncation issues when the ring is not fully covered in the image, as shown below:

$$I = \frac{\int I_{incident}}{\alpha} \tag{4.1}$$

The beam line was unfortunately somewhat unstable during our beamtime due to many uncontrollable factors, including temperature changes and vibrations. Normalizing the scattered intensity with the incident intensity can eliminate inconsistencies within the beam. It is referred to as time normalization and is defined as: I/I_0, where I_0 is the incident radiation (measured on the gold mesh, upstream from the sample) and I the scattered radiation. The incident x-ray intensity data, or time scans (see Figure 4.4 (b)), were measured in addition to the scattering images to perform this normalization.

4.4 Analysis of the Scattering Profiles

Once the normalizations are applied, a magnetic profile can be created that can immediately give information on the nanoparticle assembly's properties. The profile has a prominent peak, as can be seen in Figure 4.5, that is predominantly due to charge scattering. There is magnetic scattering information contained within the profile, but requires further

analysis and manipulation to become apparent. Both position, and the sharpness of the peak, describe the nanoparticle assembly.

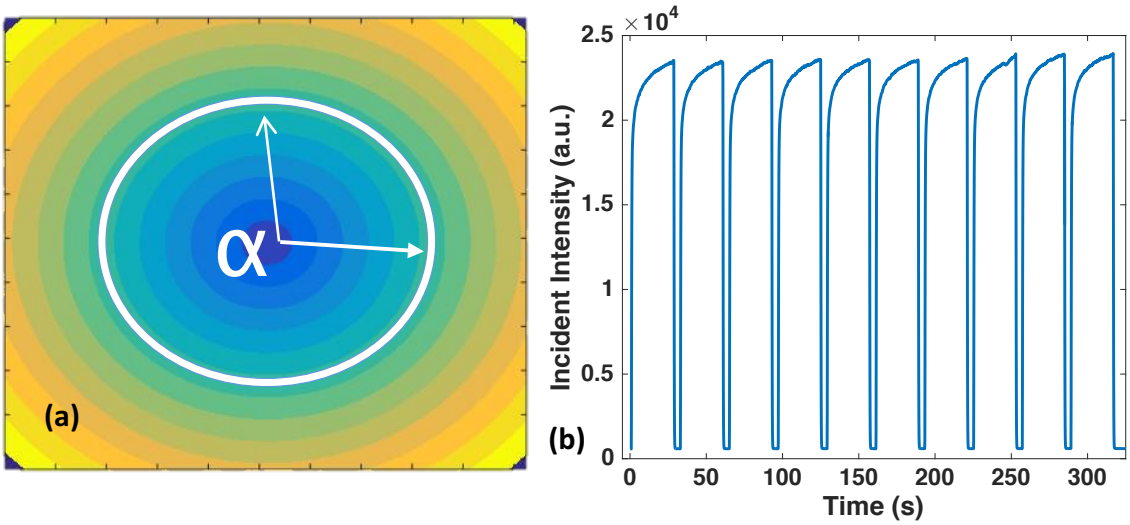

Figure 4.4 (a) Illustration of the spatial normalization. The integrated pixel intensity is divided by the angle α. **(b)** Time scan plot of integrated incident x-ray intensity as a function of time. The peaks and troughs correspond to the opening and closing of the shutter.

The peak's location gives an average distance between the nanoparticles. In order to find the average distance between the nanoparticles the peak's location must be converted from the scattering space to a physically meaningful distance. The scattering vector q can be converted to a real distance d using the Bragg diffraction law in the following manner:

$$q = \frac{2\pi}{\lambda} sin\theta \tag{4.2}$$

$$d = \frac{\lambda}{sin\theta} = \frac{2\pi}{q} \tag{4.3}$$

where *d* is the average distance between the nanoparticles, and λ is the wavelength of the soft x-rays, about 1.76 nm at the L_3 edge. The quantity $sin\theta$ is calculated by the ratio of the distance

R between the center of the beam to the ring and the distance *Z* from the sample to the CCD camera, or $\frac{R}{Z}$ (see Figure 4.5).

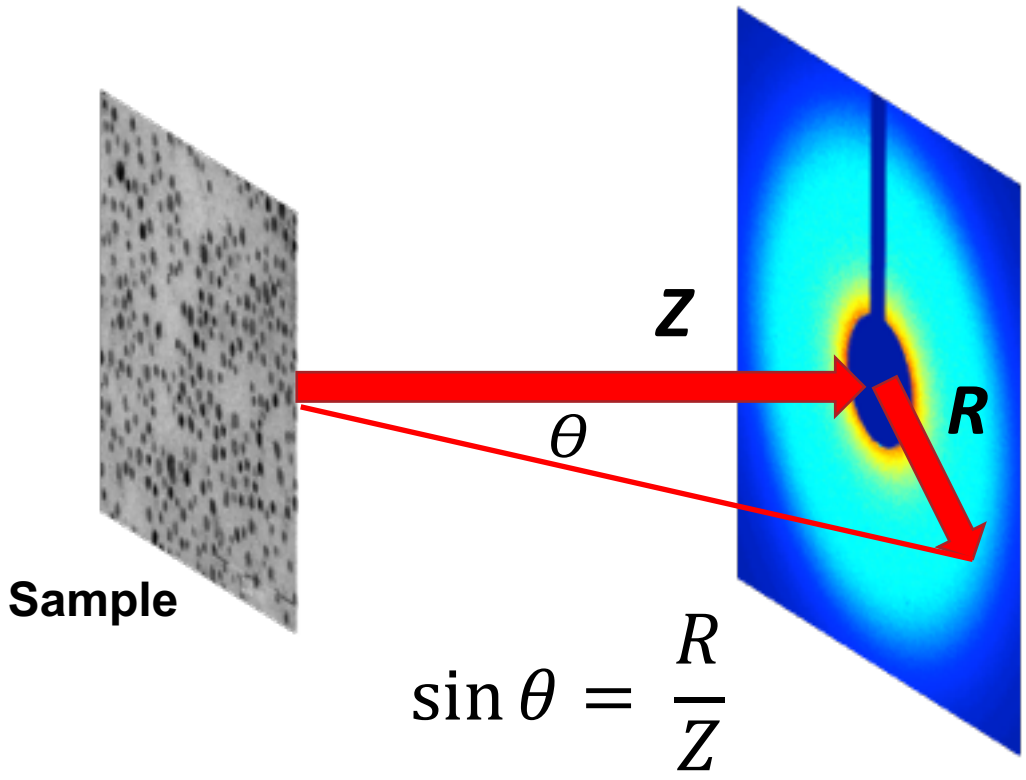

Figure 4.5 Illustration of the distance Z, measured from the sample to the CCD, and R, measured from the center of the beam to the ring in the scattering image. The ratio is used to convert the scattering vector q to a physical distance d (Equations 4.2 and 4.3).

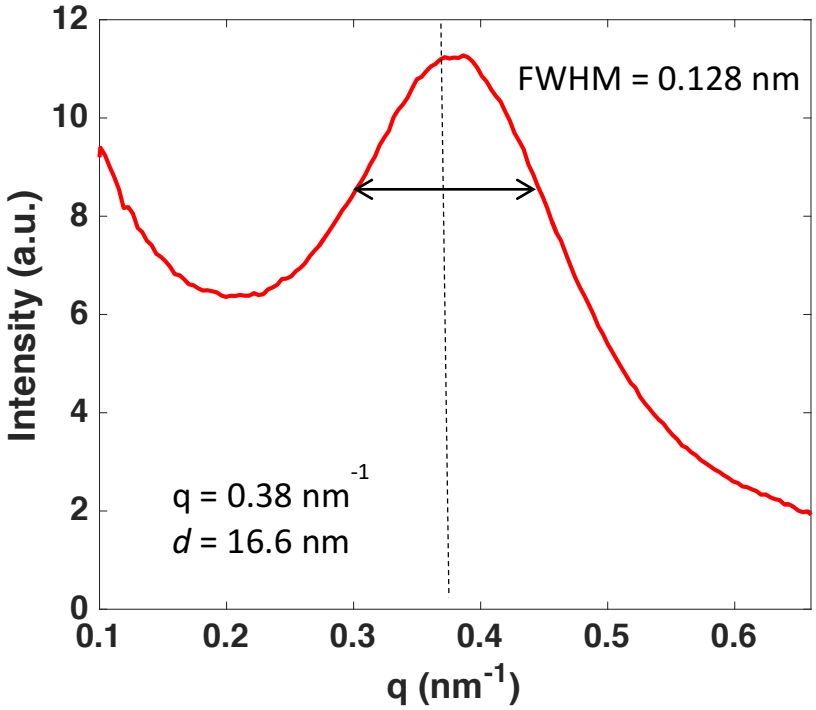

Figure 4.6 A magnetic profile for sample 3. The peak is located at q = 0.38 nm^{-1} which corresponds to an average distance of 16.6 nm between the nanoparticles in the assembly. The FWHM is also shown which describes the correlation length and order of the assembly.

The shape of the peak describes the ordering of the assembly, whether it is sparsely, or densely packed. The FWHM of the peak can be used to find the correlation length (L_c) of the samples, given $L_c = 4\pi/FWHM$. Figure 4.6 illustrates the FWHM of a profile. The FWHM is measured in the scattering space, so its inversed value represents the physical measurement. A broad peak indicates a short correlation length, or a sparser (less ordered) assembly, while a sharp peak indicates a long correlation length, or a denser (more ordered) assembly. Table 4.1 is a summary of the values attained from the magnetic profiles generated for our samples.

An illustration of interparticle distance for sample 3 is given in Figure 4.7.

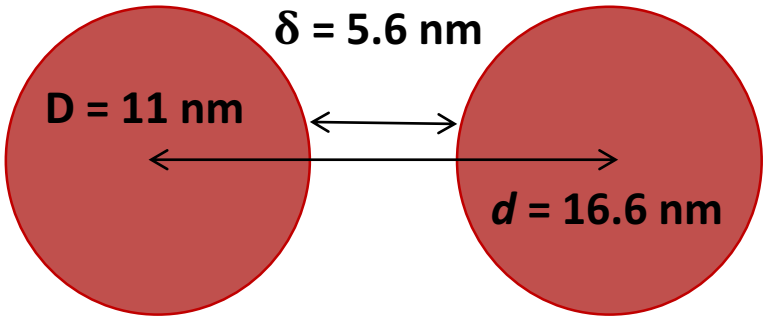

Figure 4.7 Illustration of interparticle distance for sample 3, where D is the diameter of the nanoparticle, *d* the interparticle distance (measured from the center to the center), and δ the particle spacing.

Scattering Profile Data Summary						
Sample	Set	Size (nm)	q (nm^{-1})	*d* (nm)	FWHM (nm^{-1})	L_c (nm)
1	NP16	11	0.32	19.77	0.102	122.6
2	NP16	11	0.30	20.54	0.113	110.6
3	NP16	11	0.38	16.57	0.128	98.0
7	NP18	5	1.02	6.11	0.253	49.66
8	NP18	5	1.00	6.31	0.256	49.02
9	NP18	5	1.01	6.18	0.278	45.16

Table 4.1 A summary of nanoparticle assembly data taken from magnetic profiles. From q interparticle distance *d* was calculated and from FWHM correlation length L_c was calculated. Samples 4-6 are not shown due to the weak signal in their XRMS profiles.

From the table the average interparticle distances for samples 1-3 are about twice as large as the particle diameter, which suggests a less ordered assembly. In contrast, samples 7-9 the interparticle distance is only slightly larger than the particle diameter, implying a denser and

more ordered assembly. These results can be compared, and are in reasonable agreement with the TEM images taken of the samples.

4.5 Magnetic Signal and Dichroic Effects

For this section as well, we will use sample 3 and its results as an example to understand the theory. Further analysis and discussion of sample 3, as well as our other samples, occurs in Chapter 5.

While much useful information is attained by the charge scattering analysis of the profiles, such as interparticle distance, to understand the magnetic behavior of the nanoparticle assemblies, further study is needed. By analyzing the effects of different polarizations of x-rays on the nanoparticles, magnetic properties of the assemblies can be determined. The necessity of polarized x-rays is one important reason the synchrotron at the SSRL was needed to perform our experiment. The synchrotron has undulators located at the beamline to polarize the soft x-rays into right, and left circular polarizations which will be referred to as 'positive' and 'negative' polarizations. This is critical in measuring the magnetic behavior of our samples. Figure 4.8 demonstrates the effects of polarization on sample 3 with a magnetic field near saturation. The shape and peak of the profiles remain the same, however, the intensity is affected by the different polarizations. In this case, the positive polarization shows a stronger interaction with the nanoparticles.

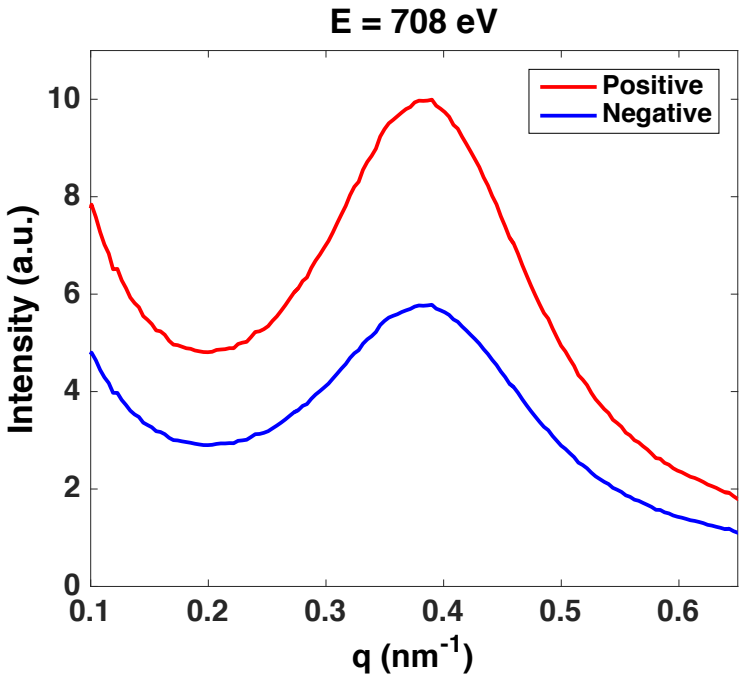

Figure 4.8 Magnetic profiles of different polarizations of sample 3 at H = 3000 G. The shape and peaks remain the same, but the intensity is changed by the different polarizations.

Remembering the XMCD results from Chapter 3, there is a distinct "W" shape (see Figure 3.4) at the L_3 edge in the absorption signal, arising from the ferrimagnetic spins of the Fe^{3+} and Fe^{2+} ions in the Fe_3O_4 nanoparticles. There is a flip in sign as we pass from E_1 (706 eV) to E_2 (707.2 eV) and then to E3 (708 eV). We expect to see this flipping in the magnetic profiles of our samples that are in an external magnetic field as we scan through these energies, as confirmation of magnetism and magnetic behavior. An exciting preliminary result, as shown in Figure 4.9 for sample 3, is that we do indeed see this flipping which confirms the magnetic behavior of our samples.

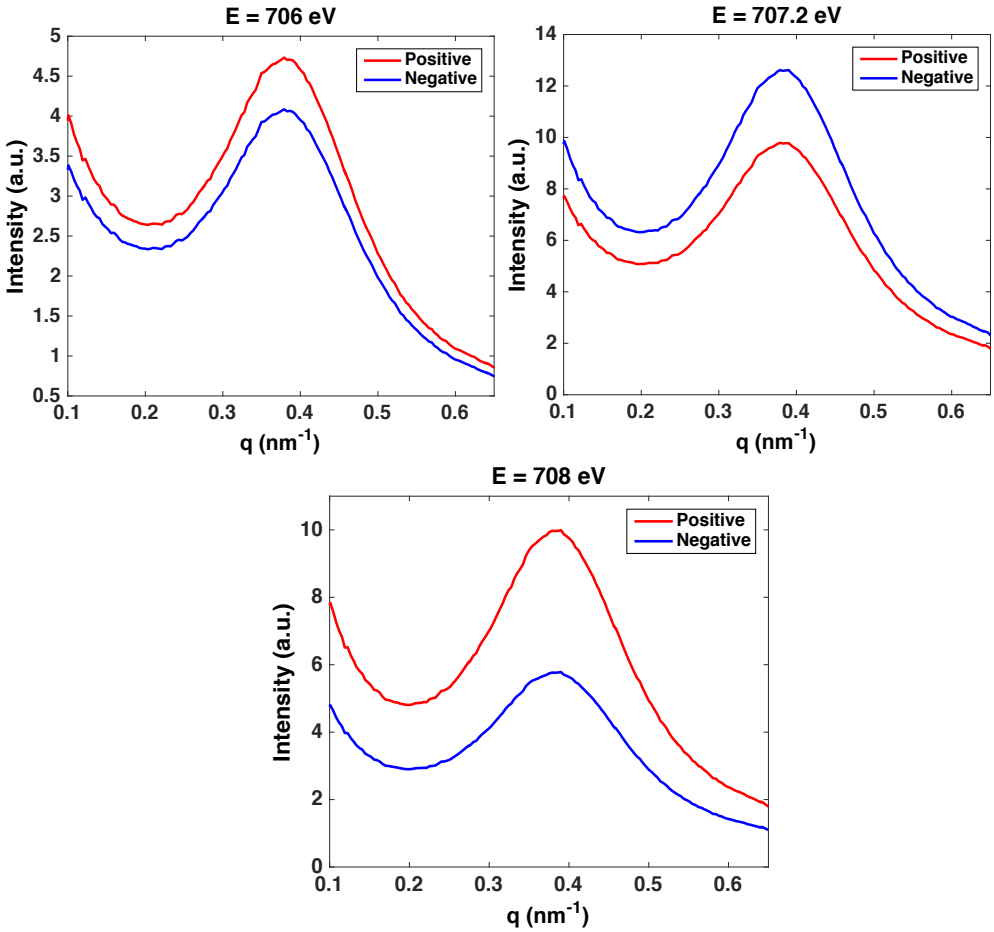

Figure 4.9 Magnetic profiles for sample 3 at H = 3000 G through the L_3 edge energies of Fe. Following the XMCD results, the polarization intensities flip at 707.2 eV, a confirmation of the magnetism and magnetic behavior in our sample.

By comparing the differences in our profiles caused by the opposite polarizations we can better understand the magnetic signal present in our profiles. In particular, the dichroic and magnetic ratios, defined in equations 4.4 and 4.5, are used to extract the magnetic signal.

$$R_D = \frac{I_+ - I_-}{I_+ + I_-} \tag{4.4}$$

$$R_M = \frac{I_+ - I_-}{\sqrt{I_+ + I_-}} \tag{4.5}$$

Figure 4.10 gives scattering profiles for sample 3 at different polarizations and the accompanying plotted dichroic and magnetic ratios.

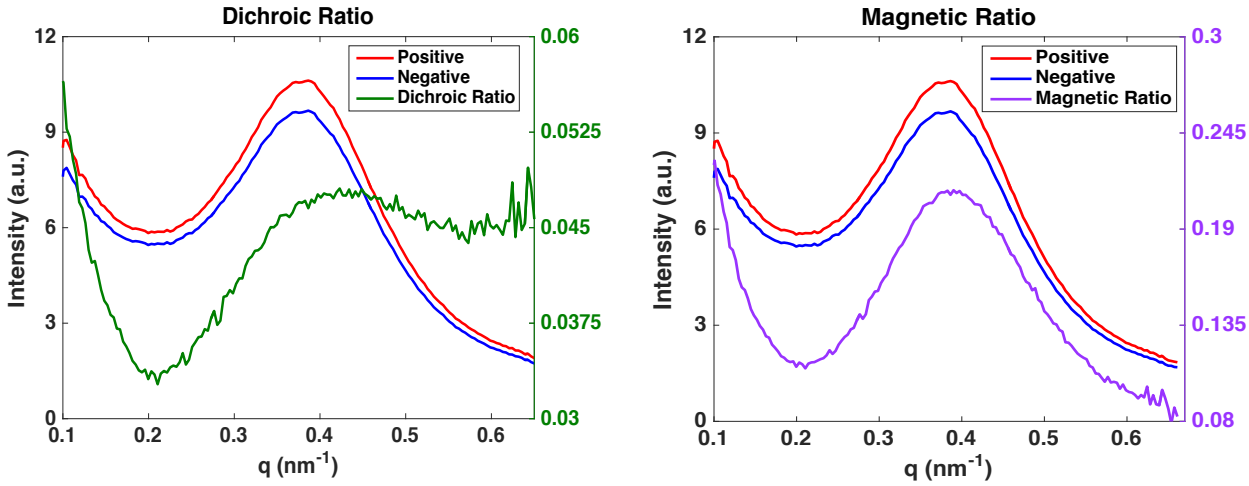

Figure 4.10 Plotted dichroic and magnetic ratios for sample 3 at H = 3000 G. The y-axes for the ratios are located along the right side. Notice the peak amplitude for the dichroic and magnetic ratios are ~ 0.05 and ~ 0.2 respectively.

A brief outline of the derivation of these ratios is given below to understand how they can be used to understand magnetic behavior. This is not an exhaustive proof, only an overview of how the ratios arise.

Atomic scattering factor with a charge and magnetic term:

$$f_{\pm} = f_c \pm f_m \tag{4.6}$$

Scattering amplitude found by a transform of the scattering factor:

$$A_{\pm}(q) = \Sigma(f_{c,j} \pm f_{m,j})e^{i\vec{q}.\vec{r}_j} = A_c \pm A_m \tag{4.7}$$

Scattering intensity, given that $A_m \ll A_c$:

$$I_{\pm} \sim |A_c|^2 \pm 2Re(A_c A_m^*) \tag{4.8}$$

Given the linear polarization signal $I_+ + I_- \sim 2|A_c|^2 \propto s_c^2$, the charge structure factor, the dichroic and magnetic ratios:

$$R_D = \frac{I_+ - I_-}{I_+ + I_-} \sim \frac{2Re(A_c A_m^*)}{|A_c|^2} \propto \frac{s_m}{s_c} \tag{4.9}$$

$$R_M = \frac{I_+ - I_-}{\sqrt{I_+ + I_-}} \sim \frac{2Re(A_c A_m^*)}{|A_c|} \propto s_m \tag{4.10}$$

where s_c and s_m are the charge and magnetic structure factors.

From the derivation above, the dichroic ratio is proportional to the ratio of the magnetic structure factor and the charge structure factor, while the magnetic ratio is proportional to the magnetic structure factor only. It is also apparent that as magnetic field decreases, both ratios decrease. If the magnetic field changes sign, the ratios will as well. Figure 4.11 demonstrates these effects for sample 3.

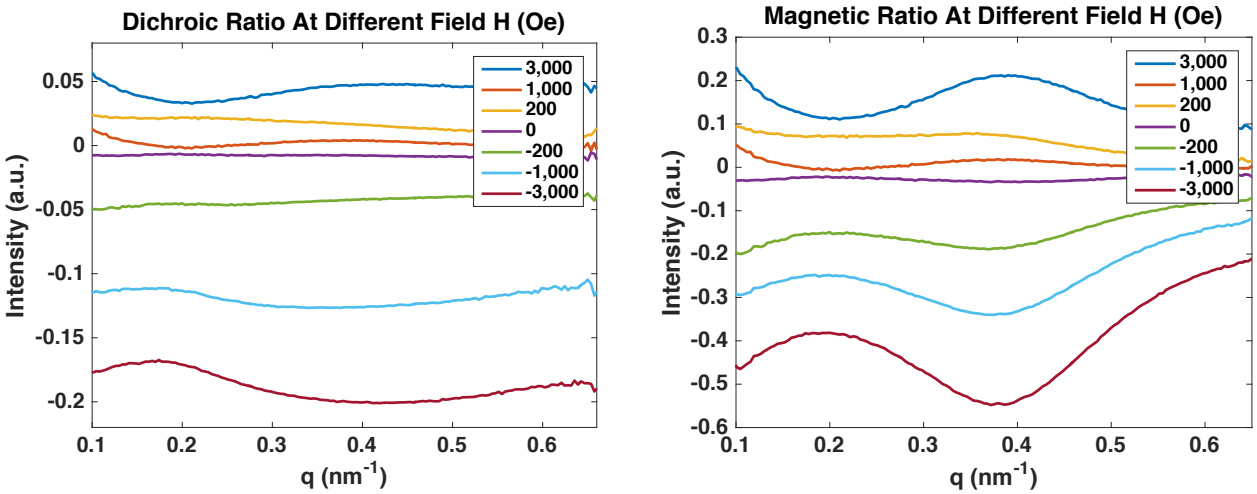

Figure 4.11 Plotted dichroic and magnetic ratios at different magnetic fields H (Oe). As the magnetic field decreases, the ratio signal decreases. As the magnetic field goes negative, the ratios flip as well.

The dichroic and magnetic ratios help isolate the magnetic behavior from the much more dominant charge scattering behavior present in the profiles. The plotted ratios can be analyzed

in much the same way the charge scattering profiles are to give information on the magnetic ordering of the nanoparticle assembly. Just like a peak indicates an average interparticle distance, or periodicity, in the charge scattering profile, a peak in the dichroic and magnetic profiles can be interpreted as the magnetic period of the nanoparticle assembly. Unlike the charge scattering peak, which remains independent of the magnetic field, the shape of the dichroic and magnetic peaks can change. This is caused by the ferromagnetic ordering in the nanoparticle assembly and can be influenced by a variety of variables including: magnetic field, and temperature. In strong magnetic fields it is expected that the magnetic ordering be mostly ferromagnetic and thus the peak position of the ratios matches the charge scattering peak. However, as the magnetic field is decreased, antiferromagnetic ordering is introduced and the magnetic periodicity changes accordingly, causing a shift in peak position.

Presentations of the analysis of our samples and the effect of temperature and magnetic field are found in the next chapter, Chapter 5.

4.6 Conclusion

Using the relatively new technique of XRMS, information about the magnetic ordering, as well as the structure of nanoparticle assemblies can be studied. In our experiment we seek to understand the effect of temperature and varying magnetic fields on our magnetite nanoparticles. We performed our experiment at SLAC, where we used a synchrotron to produce coherent, polarizable, and tunable x-rays to capture scattering images. From these scattering images, one-dimensional intensity profiles were generated that give information on the average interparticle distance in the nanoparticle assemblies. By comparing different polarizations of x-

rays using the dichroic and magnetic ratios, magnetic ordering can be studied. The next chapter will present our results.

Chapter 5

XRMS Results

5.1 Summary of Experimental Studies

In February of 2015 we carried out XRMS experiments on our freshly made nanoparticle samples. We performed two different types of studies, what we call an energy study and a field study. In our energy studies, we kept the sample in a constant magnetic field – either no field, that is 0 G, or the saturation field, that is 3000 G – and scanned the energies through the $L_{2,3}$ edges of iron (690-725 eV). Energy studies were mostly performed on sample 3 due to its strong scattering intensity. In our field studies, we fixed the energy of the x-rays to specific magnetic resonance and captured images at different magnetic field values. Both of these studies were performed at high temperature (300 K) and low temperature (10-20 K). Samples 1, 5, and 8 were not studied in depth due to their weak XMCD signal and scattering intensity.

5.2 Scattering Images

Figure 5.1 presents scattering images from all our samples. These images were captured using a CCD and used in the process described in Chapter 4 to create the scattering, magnetic, and dichroic profiles presented in the next sections. The dark blue shape through the center and extending upwards in samples 1-6, and just visible in the top right corners of samples 7-9 (these samples were offset to capture the scattering ring, which will shortly be explained), is the shadow of the blocker put in place to protect the CCD from the direct beam. Notice samples 1, 2, 4, 5, and 6 have diffuse disks surrounding the blocker, while samples 3, 7, 8, and 9 have a defined ring around the blocker. These features are indicative of sample size and assembly order. A diffuse disk, as seen in samples 1, 2, 4, 5, and 6, suggests a loose ordering, in the nanoparticle assembly. Rings, as seen in samples 3, 7, 8, and 9, indicate a periodicity, or a tighter ordering, in the nanoparticle assemblies. The radius of the ring also is significant as it provides information on the average distance between the individual nanoparticles. The CCD position for samples 7-9 were offset to capture more of the scattering ring intensity. Remembering that these images are in the scattering, or inverse space, a larger ring radius in the scattering space correlates to a smaller nanoparticle size in the real space and conversely a smaller radius to a larger nanoparticle size. The rings in the images suggest a smaller particle size for samples 7-9 as compared to sample 3, in agreement with the XRD and TEM data from Chapter 2. Samples 7-9 have an average size of 5.6 nm while sample 3 has an average size of 11.3 nm (see Table 2.1).

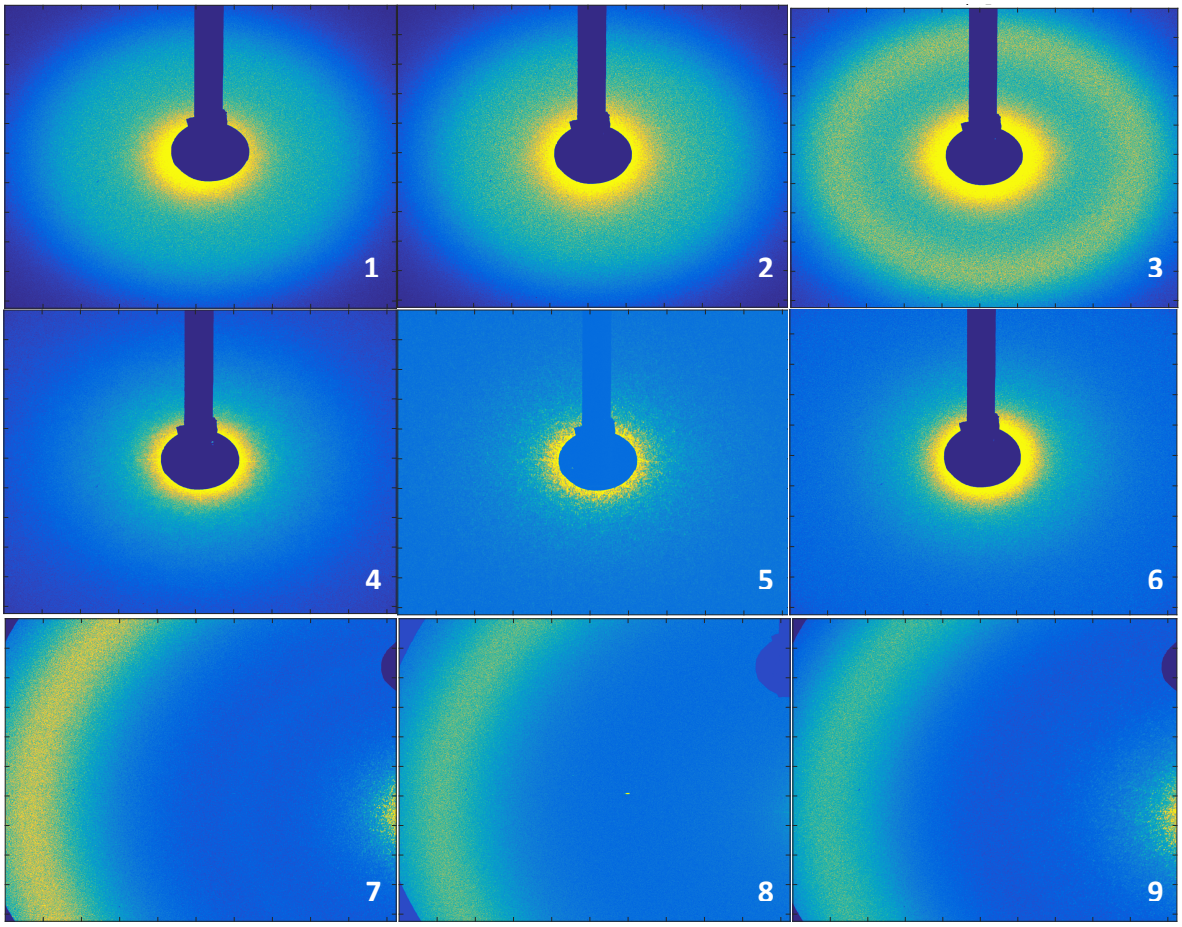

Figure 5.1 An example scattering image from all our samples, sample 1 at the top left and continuing to sample 9 at the bottom right.

5.3 Explanation of the Presentation of Experimental Results

In this section, I will present scattering profiles, dichroic ratio profiles and magnetic ratio profiles. I will first show these profiles for an energy study conducted on sample 3, at high temperature (300 K) and low temperature (10-20 K). I will then show these profiles for field studies conducted on various samples, at high and low temperatures. As explained in Chapter 4, scattering profiles are created by angularly integrating pixel intensity and plotting as a function

of q, the scattering vector. The dichroic and magnetic profiles are created by exploiting the difference in the scattering profiles for oppositely polarized x-rays (see Equations 4.4 and 4.5). The analysis presented next is preliminary with further study need to make decisive conclusions.

5.4 Energy Study at High Temperature for Sample 3

Figures 5.2 and 5.3 present scattering, dichroic, and magnetic profiles measured at the three resonance energies of sample 3 at a field H = 0 G. These resonance energies correspond to the "W" peaks in the XMCD signal (see Figure 3.4) and are E_1 = 706 eV, E_2 = 707.2 eV, and E_3 = 708 eV. The opposite polarization curves have similar intensities and the flipping from E_1 to E_2 and back to E_3 is not apparent (see Figure 4.8, Figure 5.4), a result we expect in the absence of a magnetic field. We also see very small dichroic and magnetic ratio peaks.

Figure 5.4 presents scattering, dichroic, and magnetic profiles measured at the three resonance energies of sample 3 at a field H = 3000 G. In the presence of an external magnetic field we see the splitting and flipping of the polarizations expected (see Chapter 4 for more information as to why this occurs). We also see a much stronger dichroic and magnetic signal.

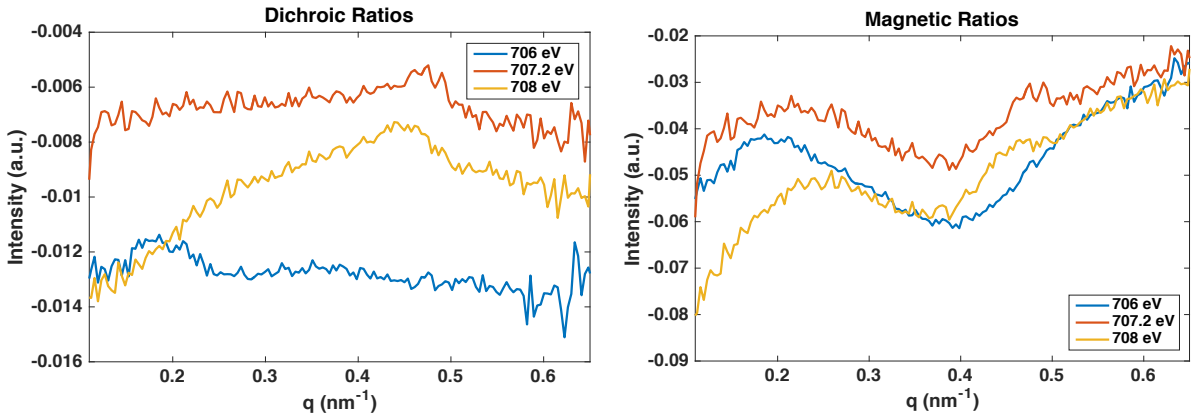

Figure 5.2 Dichroic and magnetic profiles of sample 3 at T = 300 K, H = 0 G.

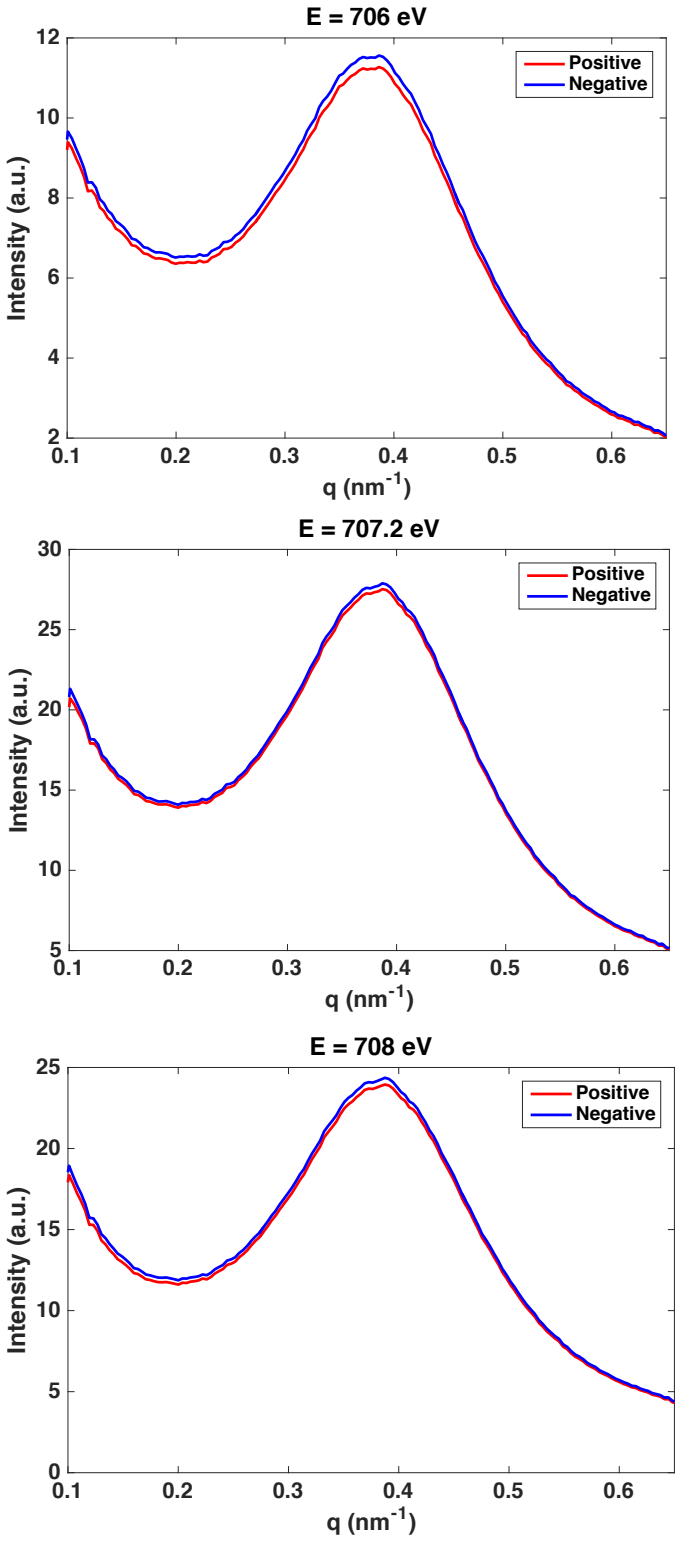

Figure 5.3 Energy study of sample 3 at T = 300 K, H = 0 G.

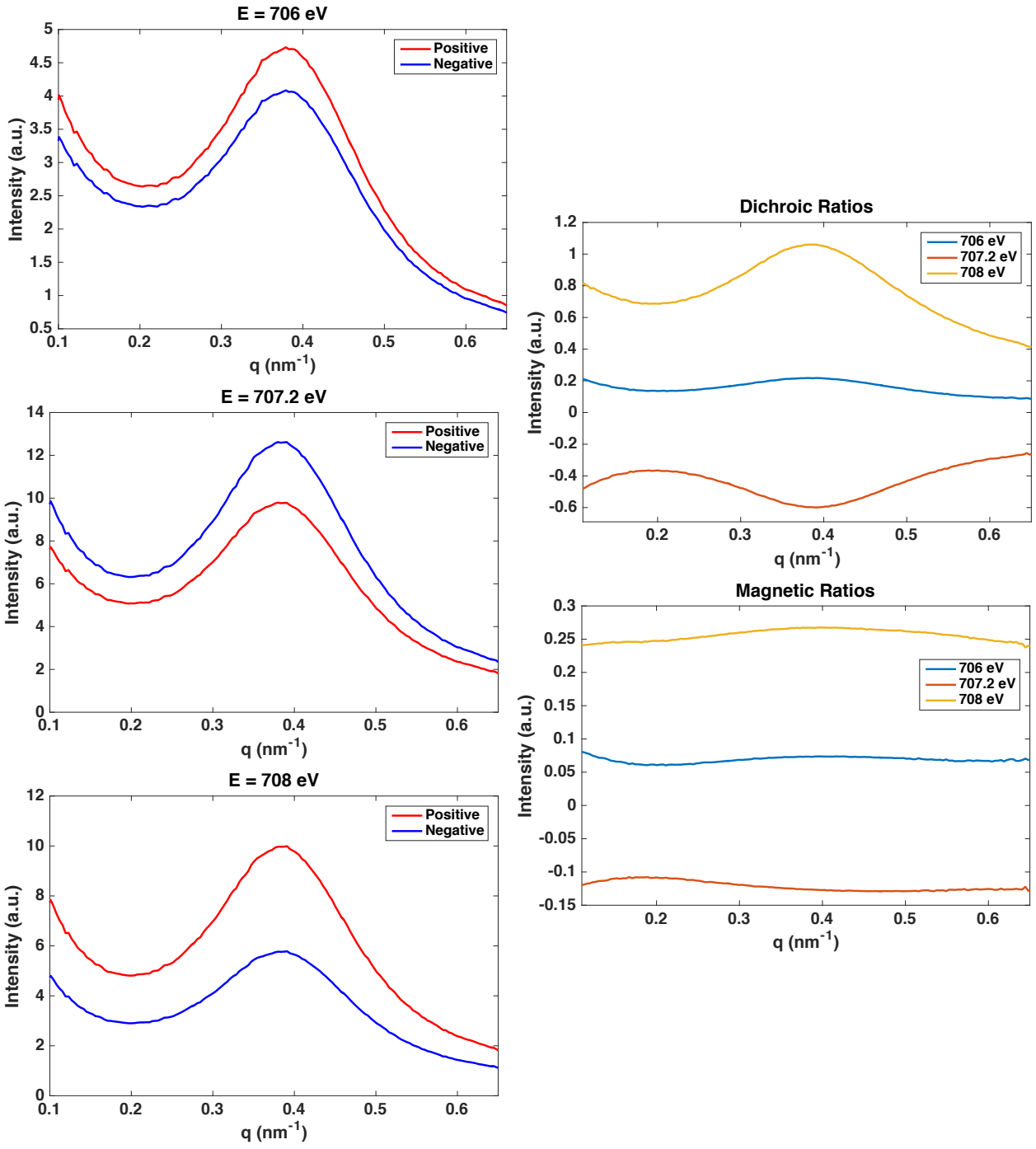

Figure 5.4 Energy study with dichroic and magnetic profiles of sample 3 at T = 300 K, H = 3000 G.

5.5 Energy Study at Low Temperature for Sample 3

Figures 5.5 and 5.6 present scattering, dichroic, and magnetic profiles measured at the three resonance energies of sample 3 at a field H = 0 G. Before and after the resonance energies we see very little scattering intensity. We do not observe splitting or flipping due to the absence of an external magnetic field.

Figure 5.7 presents scattering, dichroic, and magnetic profiles measured at the three resonance energies of sample 3 at a field H = 3000 G. Compared to the high temperature measurement with the same external magnetic field we do not clearly see the characteristic flipping from E_1 through E_3, probably due to some experimental instabilities when switching the polarization at different energies.

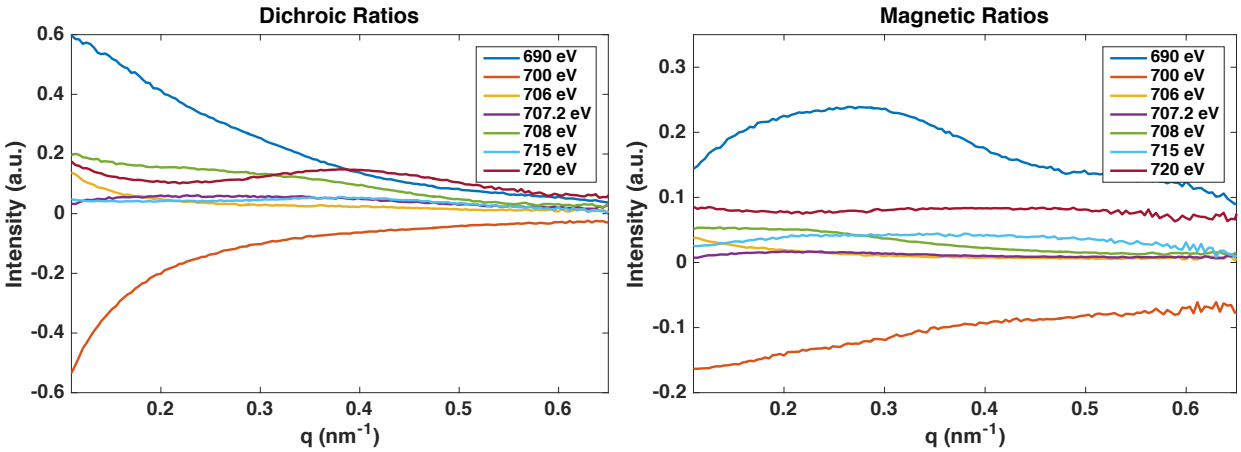

Figure 5.5 Dichroic and magnetic profiles of sample 3 at T = 0 K, H = 0 G.

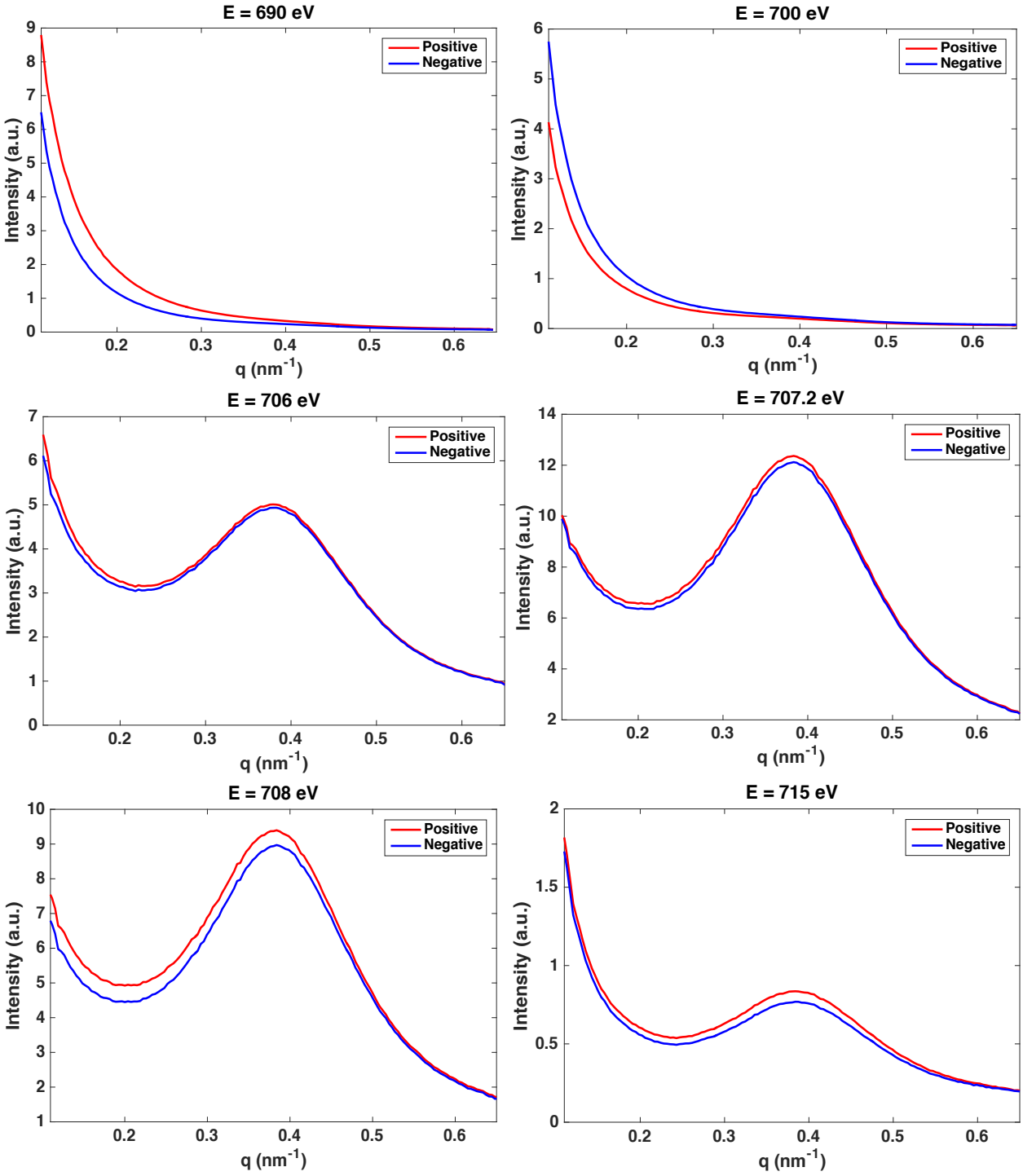

Figure 5.6 Energy study of sample 3 at T = 0 K, H = 0 G.

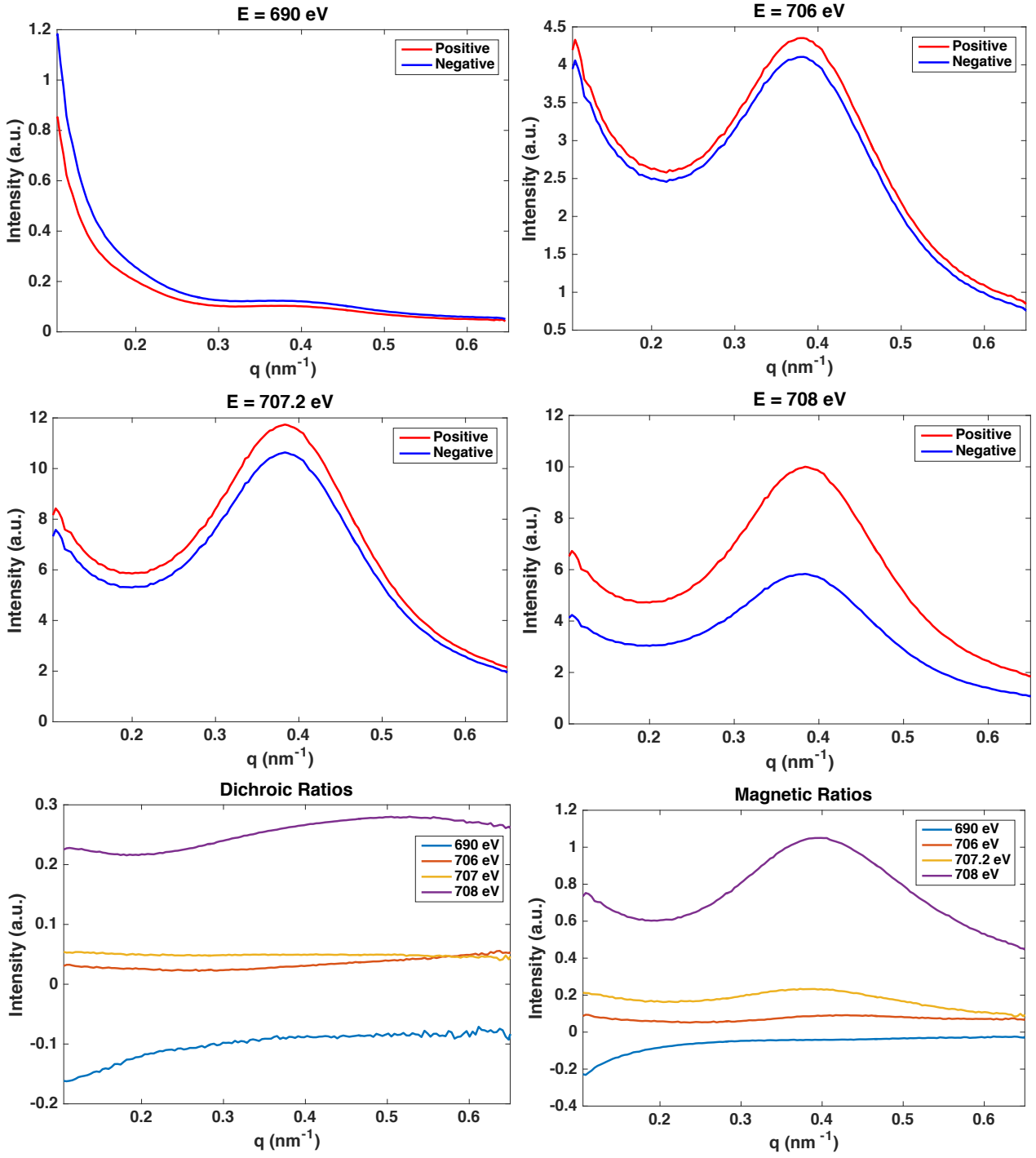

Figure 5.7 Energy study with dichroic and magnetic profiles of sample 3 at T = 0 K, H = 3000 G.

5.6 Field Study at High Temperature for Sample 2

Figure 5.8 presents scattering, dichroic, and magnetic profiles of sample 2 measured at resonance energy E_1 = 706 eV at different field values beginning at saturation H = 3000 G to H = 0 G. We see a peak intensity at the saturation field and trending down with decreasing field. We see the dichroic and magnetic profiles with the same behavior with a peak at R_D = 14% for the dichroic profile.

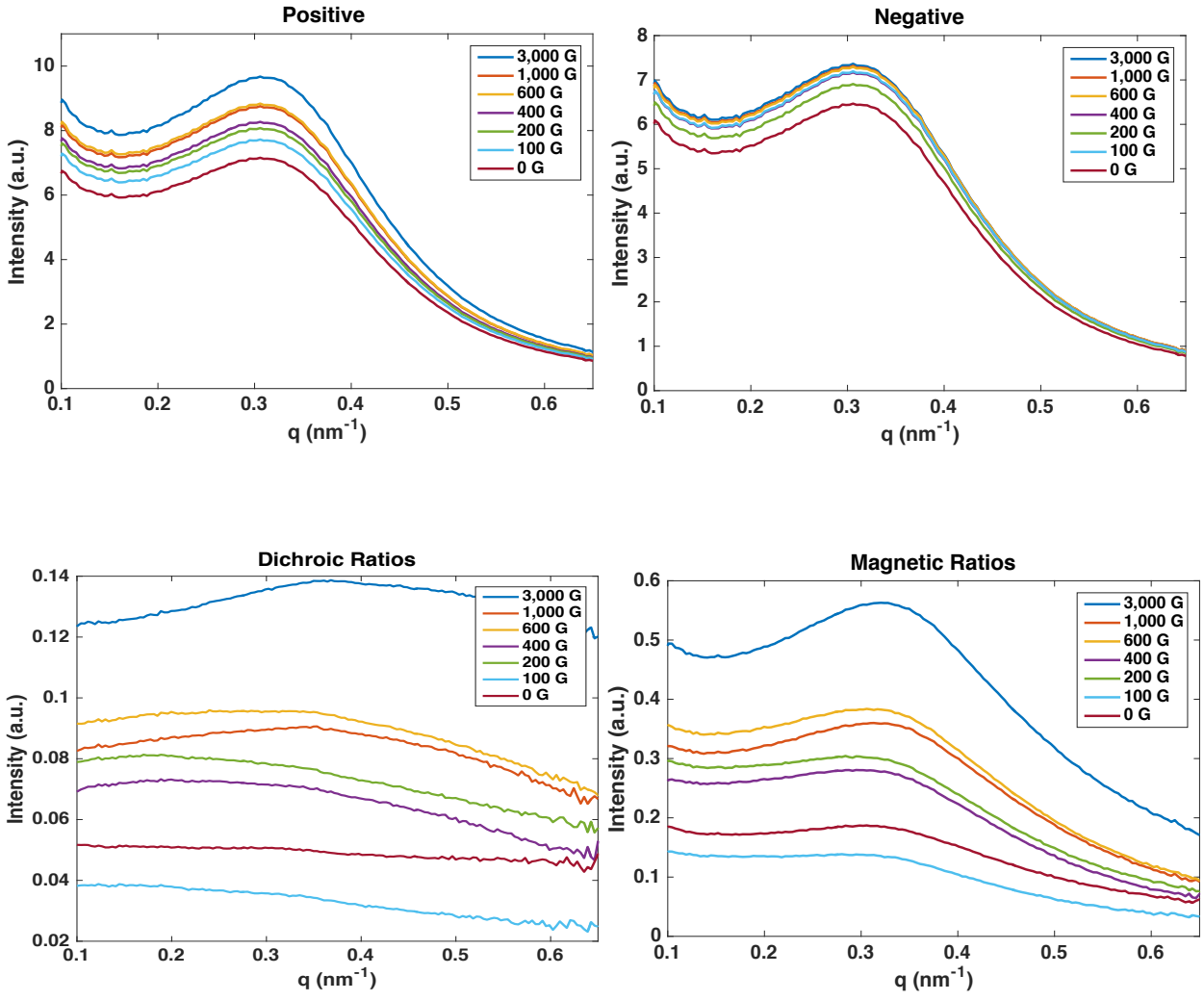

Figure 5.8 Field study with dichroic and magnetic profiles of sample 2 at T = 300 K, E = 706 eV.

5.7 Field Study at Low Temperature for Sample 2

Figures 5.9 and 5.10 present scattering, dichroic, and magnetic profiles of sample 2 measured at resonance energy E_3 = 708 eV at different field values beginning at saturation H = 3000 G to H = -3000 G. We see the same general trend, with a few random behaviors, as in the high temperature measurements. We see, roughly, less intensity at more negative field values. We also see a flipping in the dichroic and magnetic signs for negative field values.

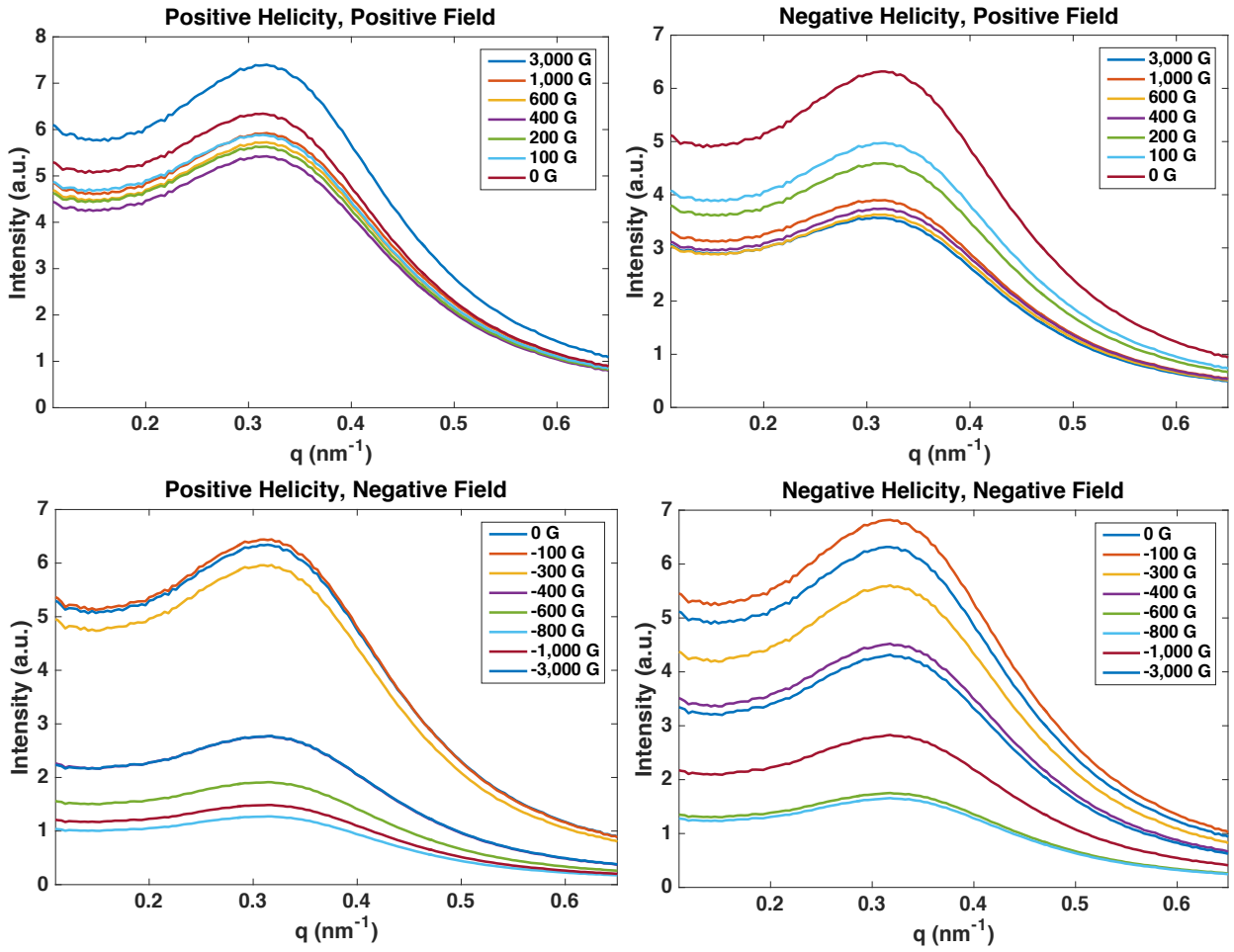

Figure 5.9 Field study of sample 2 at T = 15 K, E = 708 eV.

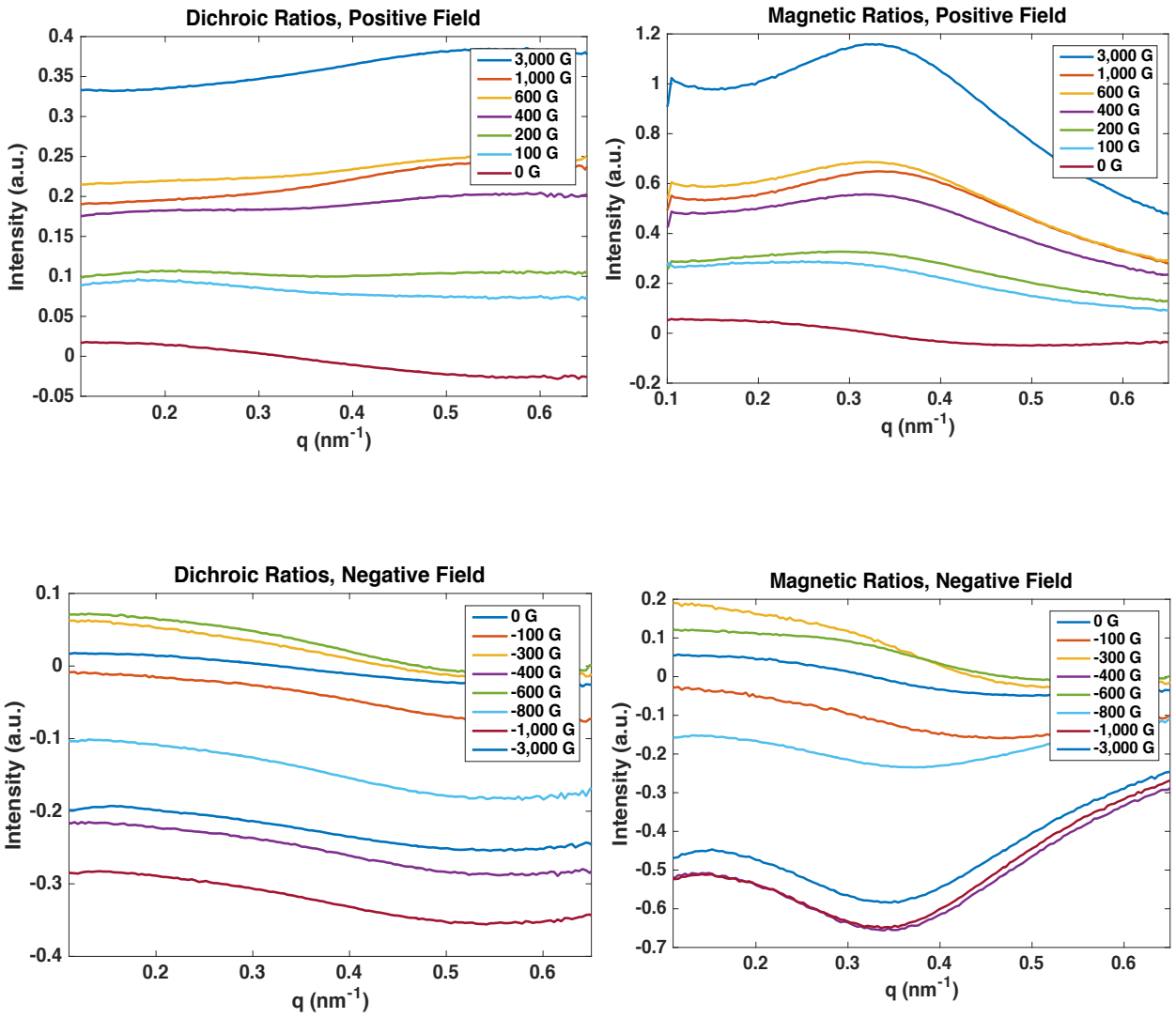

Figure 5.10 Dichroic and magnetic profiles for sample 2 at T = 15 K, E = 708 eV.

5.8 Field Study at High Temperature for Sample 3

Figures 5.11 and 5.12 present scattering, dichroic, and magnetic profiles of sample 3 measured at resonance energy E_1 = 706 eV at different field values beginning at saturation H = 3000 G to H = 0 G. We see the same correlation of higher field value to more intensity present in other samples. Particularly in this case, we see the dichroic and magnetic curves have the same shape as the scattering profiles, with prominent peaks at the same position at saturation field that then shift towards the left with decreasing field. This might suggest a change in the magnetic order of the nanoparticle samples as the external magnetic field is changed.

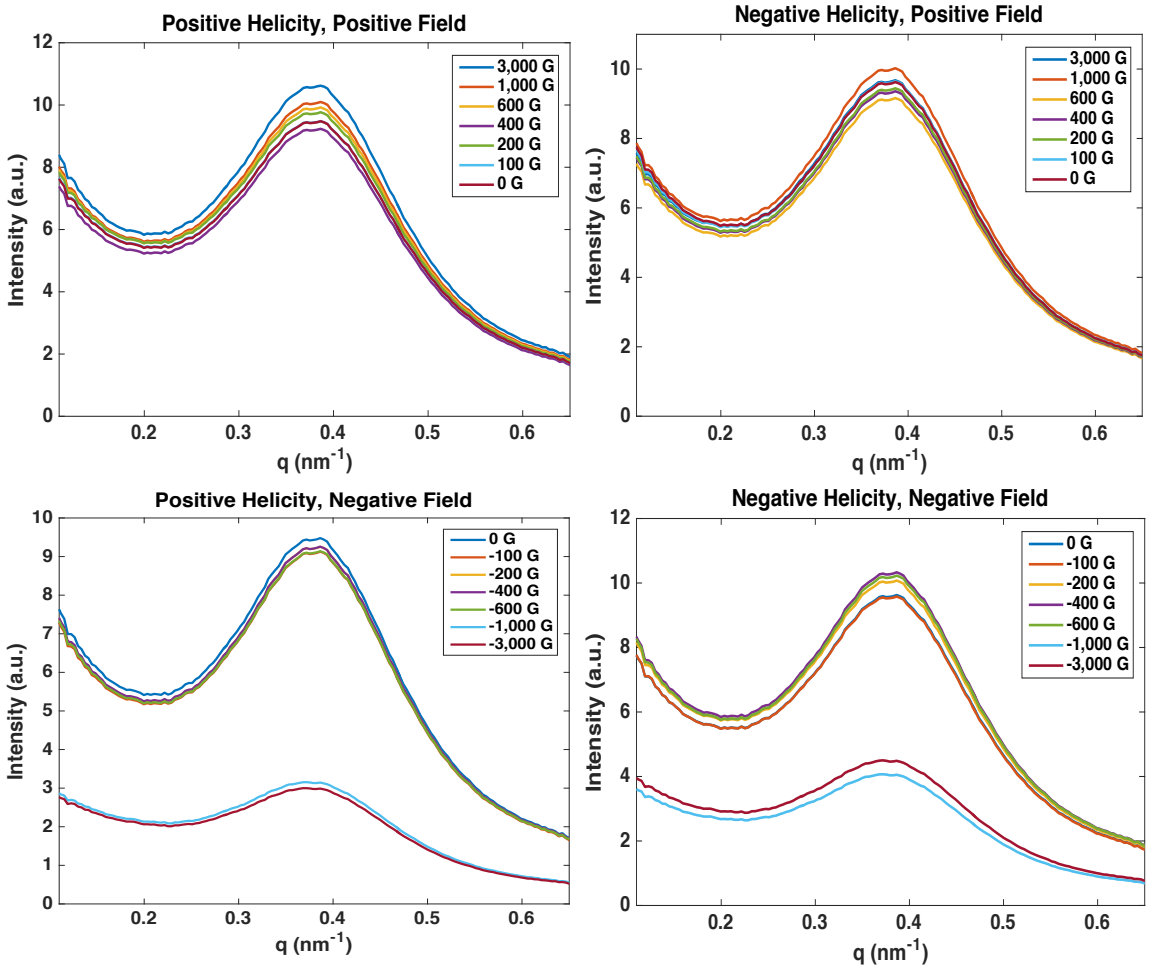

Figure 5.11 Field study of sample 3 at T = 300 K, E = 706 eV.

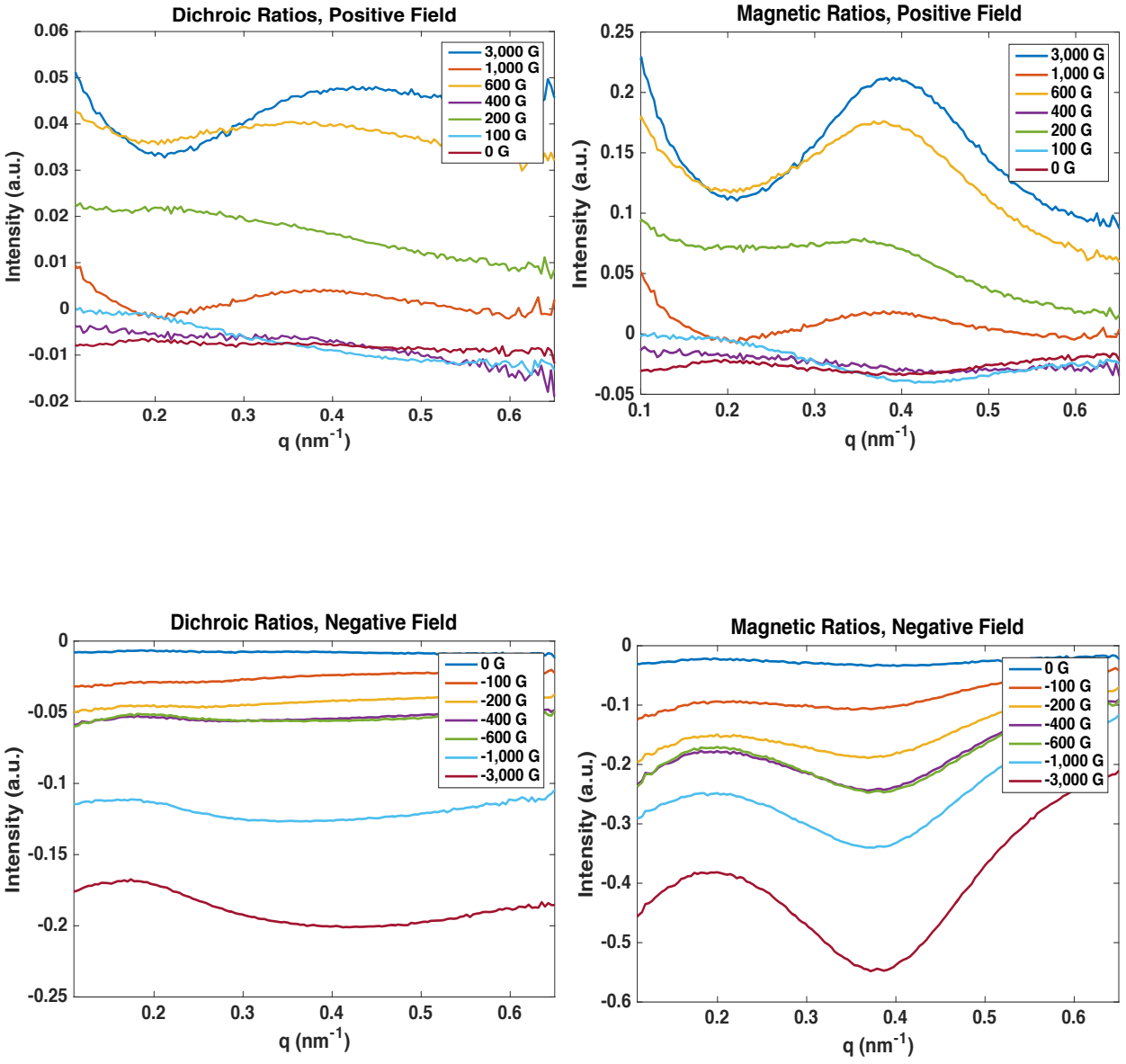

Figure 5.12 Dichroic and magnetic profiles of sample 3 at T = 300 K, E = 706 eV.

5.9 Field Study at High Temperature for Sample 4

Figure 5.13 presents scattering, dichroic, and magnetic profiles of sample 4 measured at resonance energy E_1 = 706 eV at different field values beginning at saturation H = 3000 G to H = 0 G. Compared to samples 1 and 3, sample 4 has a much weaker scattering signal, but a peak is visible nevertheless.

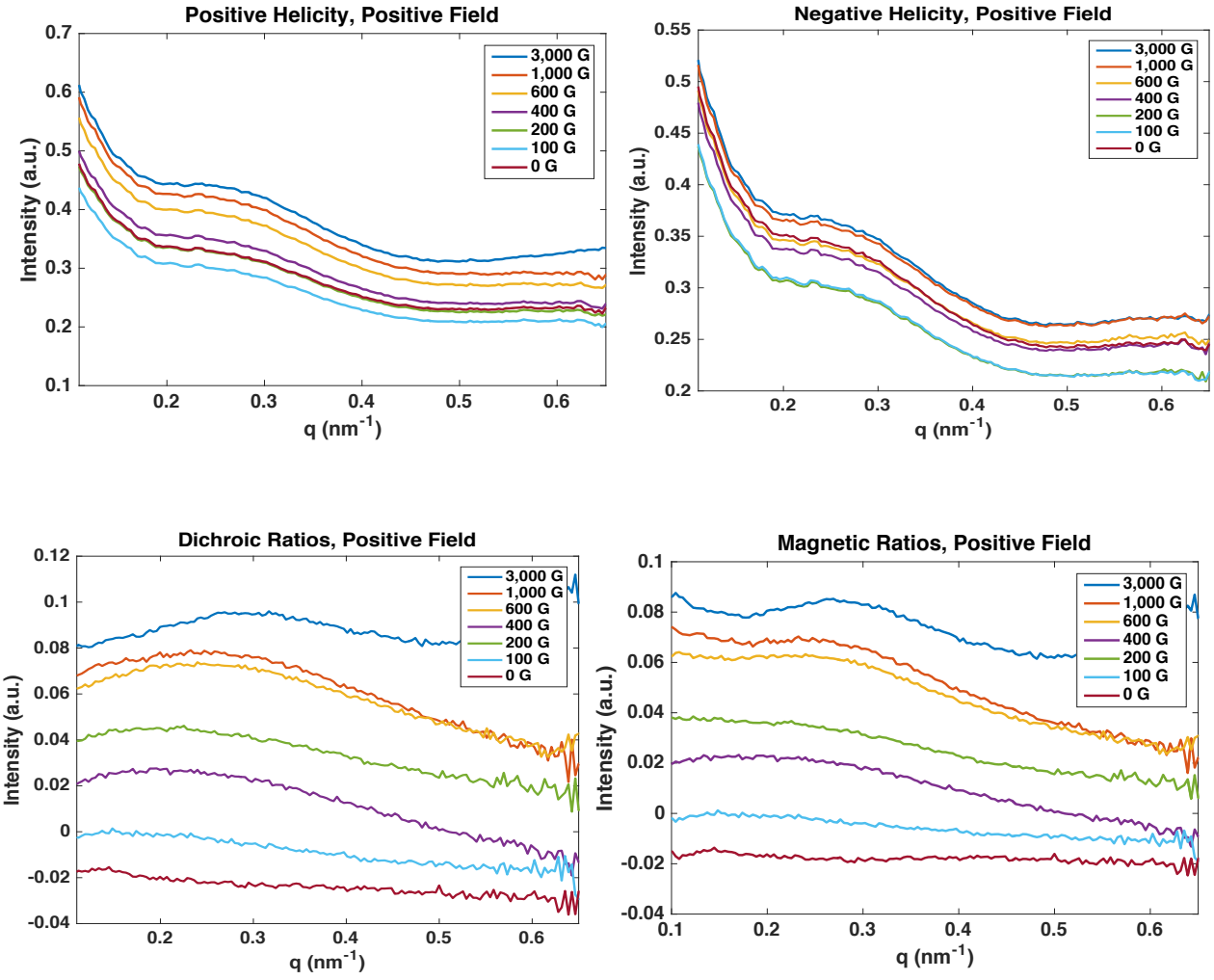

Figure 5.13 Field study with dichroic and magnetic profiles of sample 4 at T = 300 K, E = 706

5.10 Field Study at High Temperature for Sample 6

Figure 5.14 presents scattering, dichroic, and magnetic profiles of sample 6 measured at resonance energy E_1 = 706 eV at different field values beginning at saturation H = 3000 G to H = 0 G. Sample 6 also has a relatively weak signal.

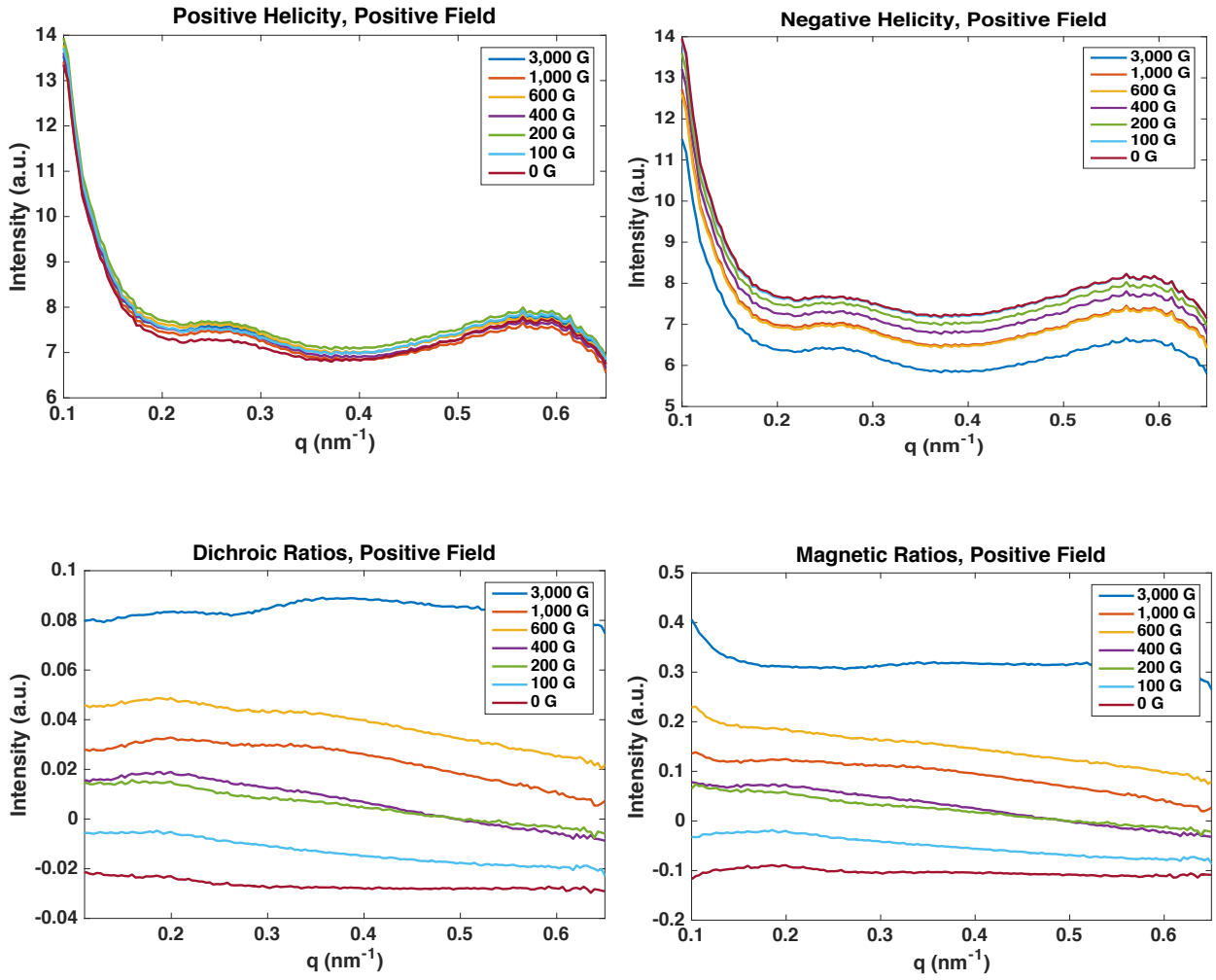

Figure 5.14 Field study with dichroic and magnetic profiles of sample 6 at T = 300 K, E = 706 eV.

5.11 Field Study at Low Temperature for Sample 6

Figures 5.15 and 5.16 present scattering, dichroic, and magnetic profiles of sample 6 measured at resonance energy E_3 = 708 eV at different field values beginning at saturation H = 3000 G to H = -3000 G. Compared to the high temperature measurements the secondary peak has vanished. We see a strong dichroic and magnetic signal, up to 60%.

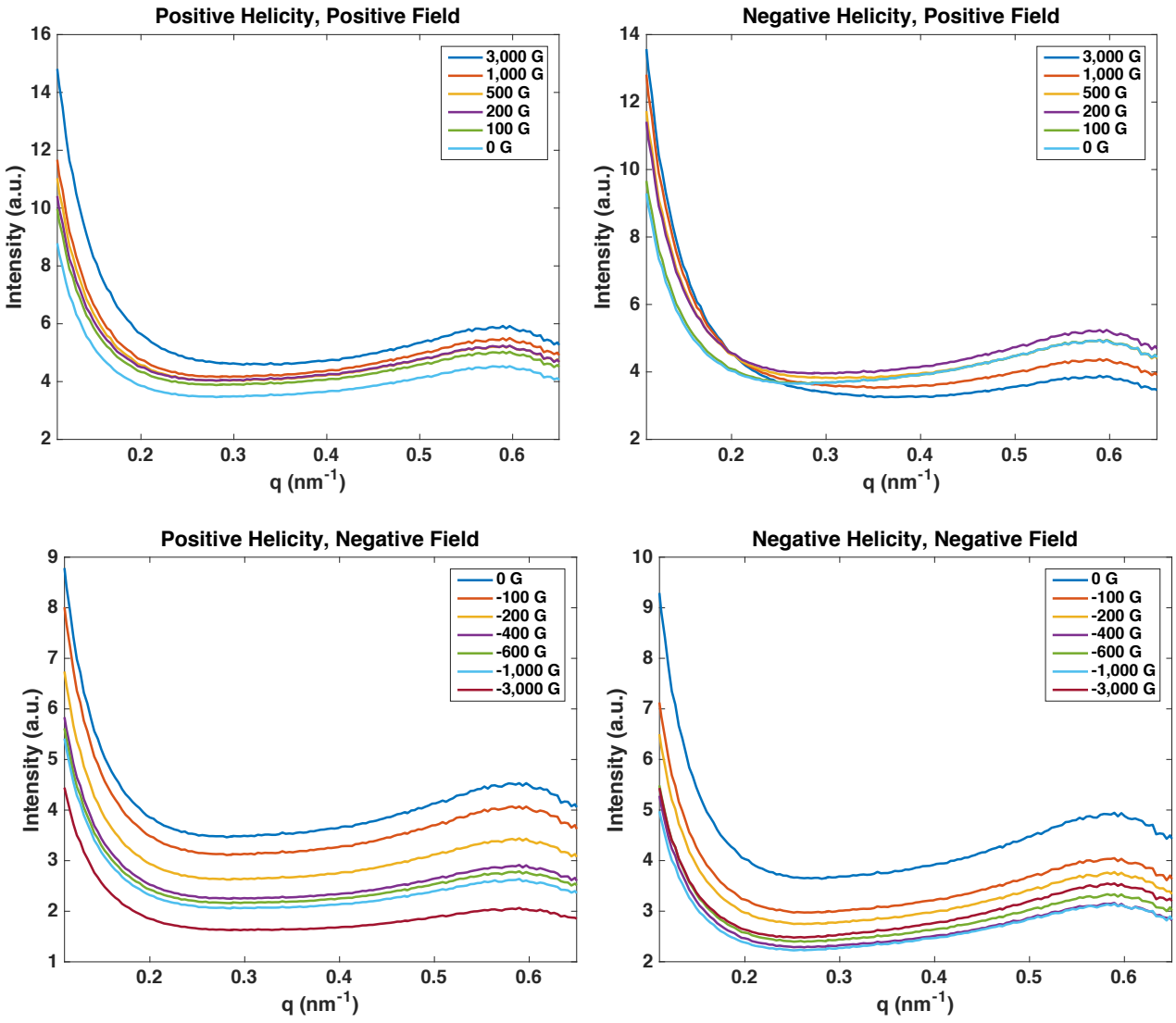

Figure 5.15 Field study of sample 6 at T = 15 K, E = 708 eV.

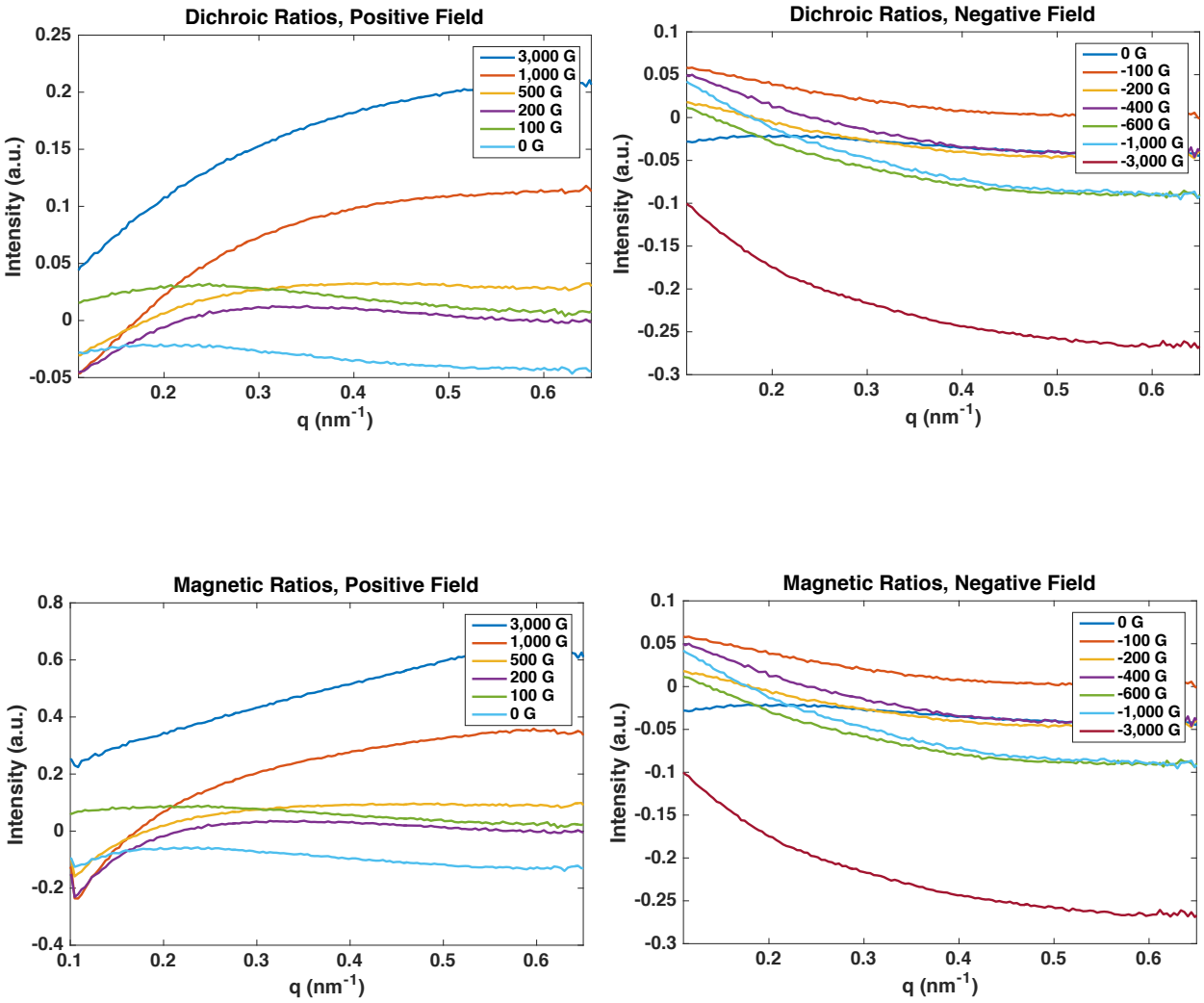

Figure 5.16 Dichroic and magnetic profiles of sample 6 at T = 15 K, E = 708 eV.

5.12 Field Study at High Temperature for Sample 7

Figure 5.17 presents scattering, dichroic, and magnetic profiles of sample 7 measured at resonance energy E_1 = 706 eV at different field values beginning at saturation H = 3000 G to H = 0 G. We see a peak at a higher q compared to the previous samples due to the CCD being shifted off center to capture the scattering ring. We see strong dichroic signal, as much as 10%. Magnetic signal seems to be inverted, a feature that requires further study.

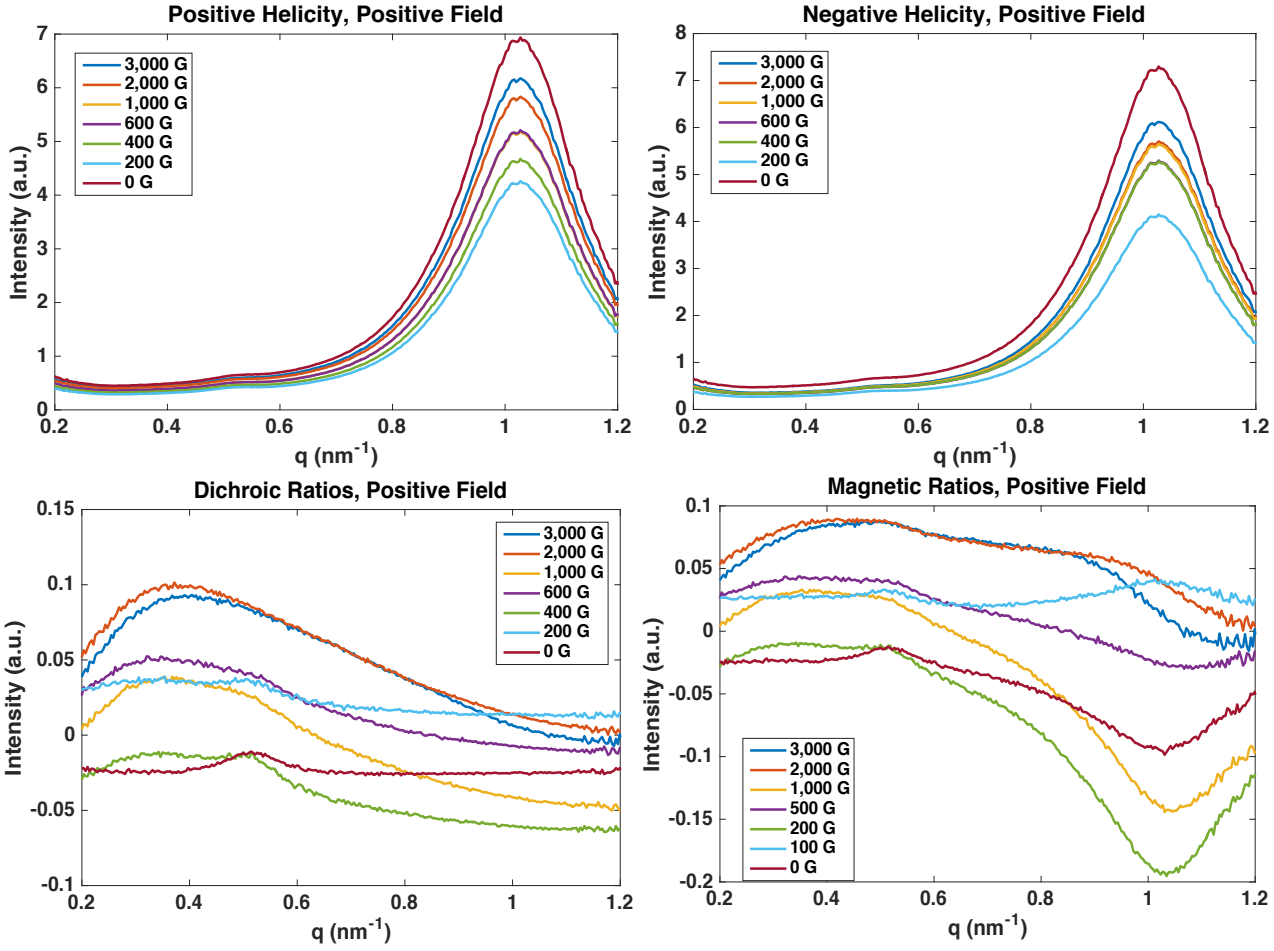

Figure 5.17 Field study with dichroic and magnetic profiles of sample 7 at T = 300 K, E = 706 eV.

5.13 Field Study at Low Temperature for Sample 7

Figure 5.18 presents scattering, dichroic, and magnetic profiles of sample 7 measured at resonance energy E_1 = 706 eV at different field values beginning at saturation H = 3000 G to H = 0 G. The same inverting of the magnetic signal is manifested in the low temperature results as well.

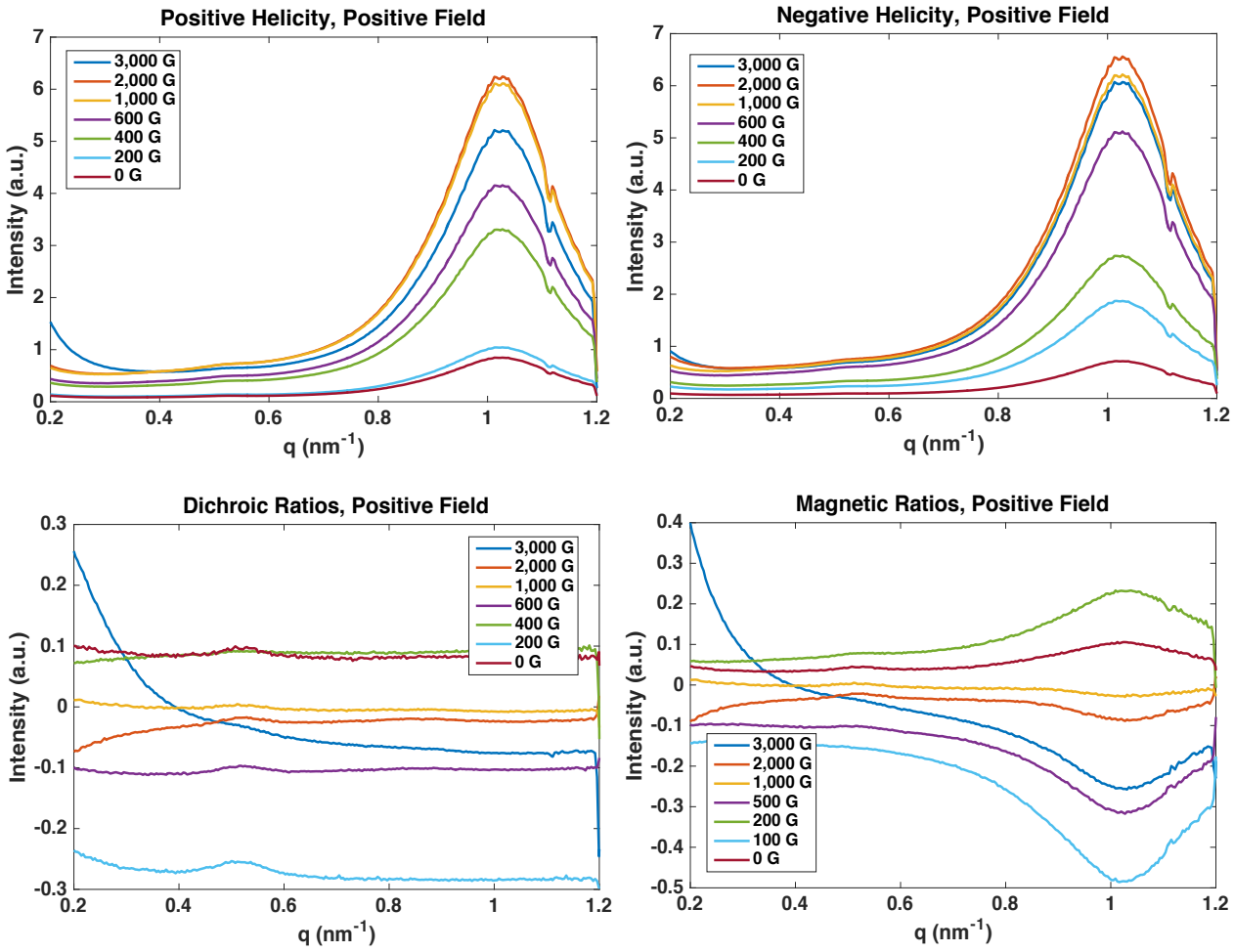

Figure 5.18 Field study with dichroic and magnetic profiles of sample 7 at T = 15 K, E = 706 eV.

5.14 Field Study at High Temperature for Sample 9

Figure 5.19 presents scattering, dichroic, and magnetic profiles of sample 9 measured at resonance energy E_1 = 706 eV at different field values beginning at saturation H = 3000 G to H = 0 G. Sample 9 has the same shape as sample 7 as it was shifted in the same manner. We see no obvious peaks in the dichroic profiles but for H = 3000 G, we see a peak in the magnetic profile at the same location as the peak in the scattering profile which gradually dissipates as the field is decreased.

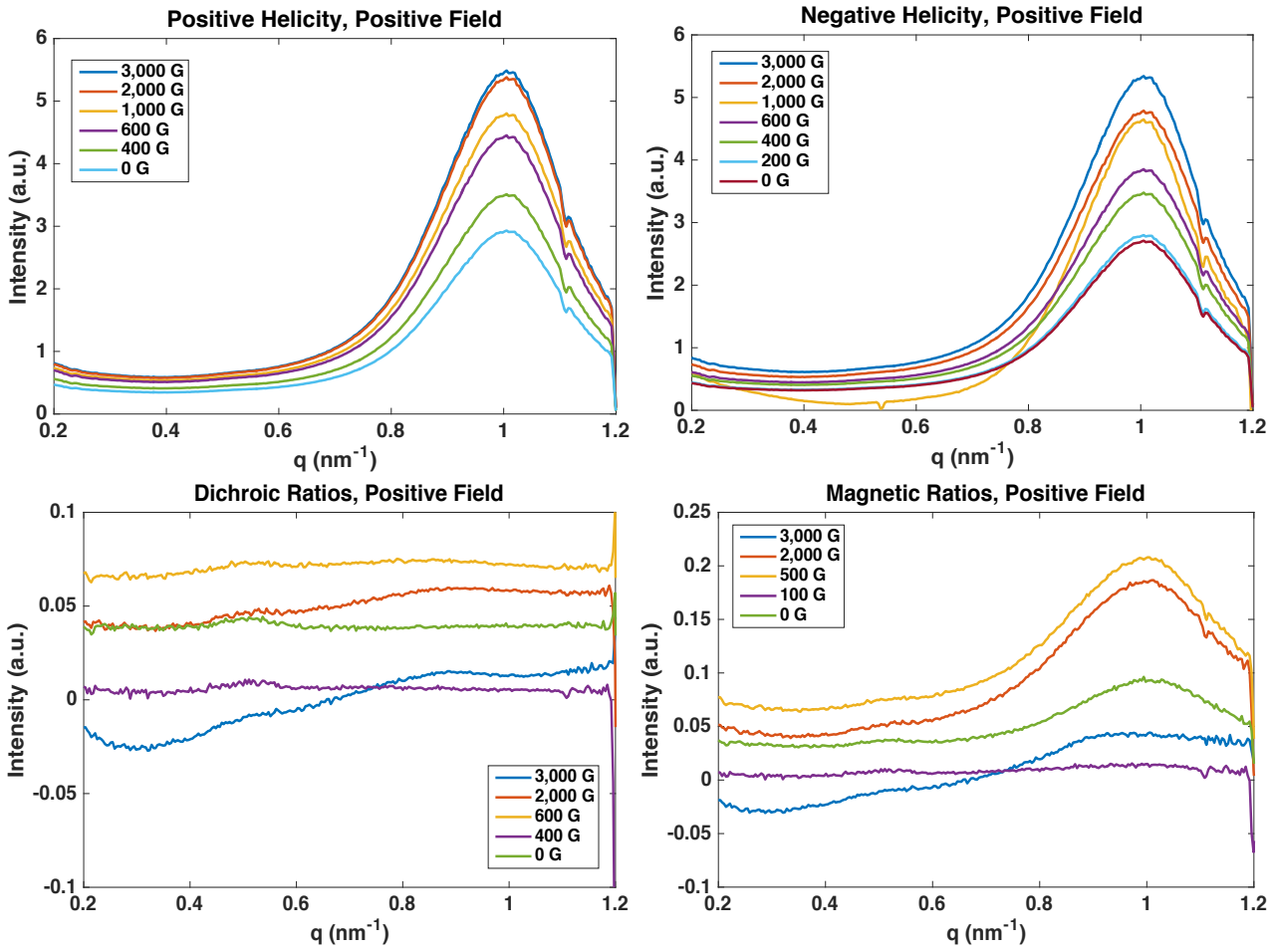

Figure 5.19 Field study with dichroic and magnetic profiles of sample 9 at T = 300 K, E = 706 eV.

5.15 Field Study at Low Temperature for Sample 9

Figure 5.20 presents scattering, dichroic, and magnetic profiles of sample 9 measured at resonance energy E_1 = 706 eV at different field values beginning at saturation H = 3000 G to H = 0 G. Compared to the high temperature results we see a stronger peak shape in the dichroic signal, about 16% at a maximum.

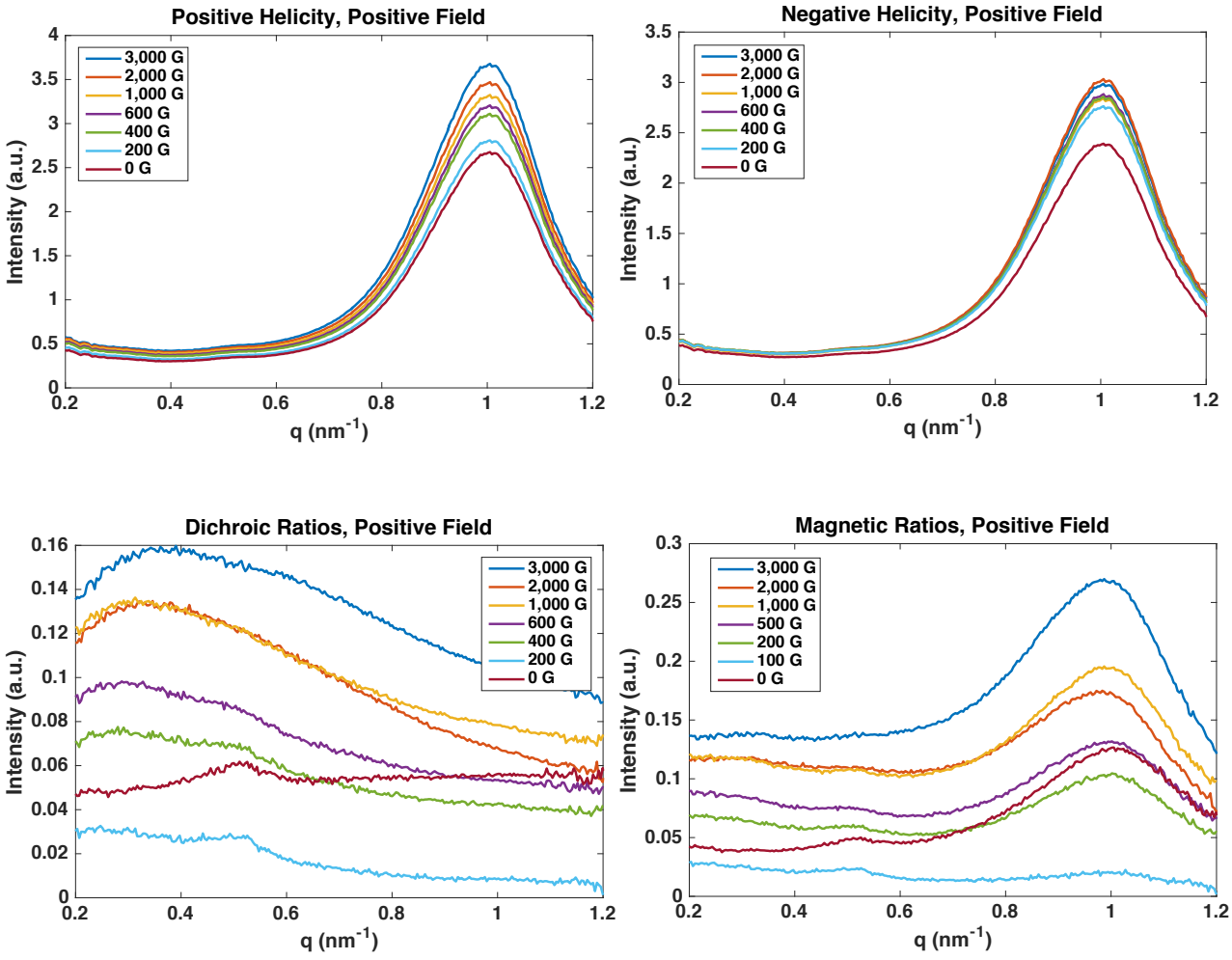

Figure 5.20 Field study with dichroic and magnetic profiles of sample 9 at T = 15 K, E = 706 eV.

5.16 Discussion

Much of my work on this project went into the study and process of creating these scattering, dichroic, and magnetic profiles presented in this chapter. Analysis of these profiles is still ongoing. As with any experiment, there are many factors, external and internal, to consider when drawing conclusions based on data. In light of these preliminary results, we start to see a trend in the magnetic behavior between the smaller and larger particles. These observations are currently being supported by numerical simulations based on chains of nanoparticle where various magnetic orders are incorporated.

Chapter 6

Conclusion

Magnetic nanoparticle technology is changing the world with seemingly endless applications. For example, magnetic nanoparticles, particularly magnetite, are helping to create more effective cancer treatments. Understanding the magnetic behavior of these nanoparticles is essential to progress and innovations in these treatments and many other applications.

To better understand the magnetic properties of magnetite (Fe_3O_4) we prepared magnetite nanoparticle assemblies using organic methods (see Chapter 2). We found that by controlling temperature and reaction solutions we can directly influence the individual nanoparticle size. We successfully created three nanoparticle sets with differing nanoparticle sizes ranging from 5-11 nm. By applying different concentrations of our nanoparticles to a Si_3N_4, we created nine different nanoparticle samples. Using XRD and TEM we measured our average nanoparticle size.

Using our freshly made samples we carried out XMCD and XRMS experiments using the synchrotron at SLAC. Using XMCD techniques we found absorption peaks at the $L_{2,3}$ edge of iron, confirming the chemical makeup of our samples to be Fe_3O_4 (see Chapter 3). Using XRMS techniques we isolated magnetic scattering, using the dichroic and magnetic ratios, and saw flipping in the magnetic profiles as we scanned through the $L_{2,3}$ edge of iron (Fe), confirmation of the magnetic nature of the signal and providing information about the magnetic behavior in our samples (see Chapter 4).

Much more information is yet to be studied and many conclusions made from the vast amount of data collected in our experiments. It remains a work in progress including numerical simulation of the magnetic ordering. This thesis helped in gathering our experimental results and in drawing important preliminary conclusions.

Bibliography

[1] Singh, Rajesh, and James W. Lillard. “Nanoparticle-Based Targeted Drug Delivery.” Experimental and Molecular Pathology **86(3)**: 215–223, (2009).

[2] Roussakow, Sergey. "The History of Hyperthermia Rise and Decline". Conference Papers in Medicine 1–40, (2013).

[3] Mohr, R.; Kratz, K.; Weigel, T.; Lucka-Gabor, M.; Moneke, M.; Lendlein, A. "Initiation of shape-memory effect by inductive heating of magnetic nanoparticles in thermoplastic polymers". Proceedings of the National Academy of Sciences of the United States of America **103**: 3540–3545, (2010).

[4] A. Ito, M. Shinkai, H. Honda, and T. Kobayashi, “Medical Application of Functionalized Magnetic Nanoparticles,” J. Biosci. Bioeng **100**: 1, (2005).

[5] Spaldin, Nicola A. "Ferrimagnetism". Magnetic Materials: Fundamentals and Applications (2nd ed.), 113–129, (2010).

[6] Cai, Y. P., et al. “Spin and Orbital Moments and Magnetic Order in Fe3O4 Nanoparticle Assemblies.” Journal of Applied Physics, **115**: 17B537, (2014).

[7] P. Guardia, N. Prez, A.Labarta, and X. Batlle, “Controlled Synthesis of Iron Oxide Nanoparticles over a Wide Size Range,” Langmuir, **26(8):** 5843, (2010).

[8] P. Guardia, J. Prez-Juste, A. Laharte, X. Batlle, and L. M. Liz-Marzn, “Heating Rate Influence On the Synthesis of Iron Oxide Nanoparticles: the Case of Decanoic Acid,” Chem. Commun, **46**: 6108, (2010).

[9] N. R. Jana, Y. F. Chen, and X. G. Peng, “Size- and Shape-Controlled Magnetic (Cr, Mn, Fe, Co, Ni) Oxide Nanocrystals via a Simple and General Approach,” Chem. Mater., **16**: 3931, (2004).

[10] C. Altavilla, E. Ciliberto, D. Gatteschi, and C. Sangregorio, “A New Route to Fabricate Monolayers of Magnetite nano particles on Silicon,” Advanced Materials, **17(8)**: 1084, (2005).

[11] K. Chesnel, M. Trevino, Y. Cai, J. Hancock, S. Smith, and R., Harrison, "Particle Size Effects On the Magnetic Behavior of 5 to 11 nm Fe3O4 Nanoparticles," Journal of Physics: Conf. Series, **521**: 012004, (2014).

[12] P. Platzman and N. Tzoar, “Magnetic Scattering of X Rays from Electrons in Molecules and Solids,” Phys. Rev., **B(2)**: 3556, (1970).

[13] F. de Bergevin and M. Brunel, “Diffraction of X-rays by Magnetic Materials. I. General Formulae and Measurements on Ferro- and Ferrimagnetic Compounds,” Acta Cryst., **A(37)**: 314, (1981).

[14] G. van der Laan and B. T. Thole, “Strong Magnetic X-ray Dichroism In 2p Absorption Spectra of 3d Transition-metal Ions,” Phys. Rev., **B(43)**: 13401, (1991).